JGR Oceans

RESEARCH ARTICLE
10.1029/2020JC017069

Drivers of Phytoplankton Blooms in Hawaii: A Regional Model Study

T. Friedrich[1,2], B. S. Powell[1], C. A. Stock[3], L. Hahn-Woernle[4], R. Dussin[3], and E. N. Curchitser[5]

[1]Department of Oceanography, University of Hawaii at Mānoa, 1000 Pope Road, MSB 205, Honolulu, HI, USA, [2]Pacific Islands Ocean Observing System (PacIOOS), Honolulu, HI, USA, [3]NOAA/Geophysical Fluid Dynamics Laboratory, Princeton, NJ, USA, [4]Joint Institute for Marine and Atmospheric Research, University of Hawaii at Mānoa, Honolulu, HI, USA, [5]Department of Environmental Sciences, Rutgers University, New Brunswick, NJ, USA

Key Points:

- A new high-resolution physical-biogeochemical model of Hawaii compares well with observations
- Phytoplankton blooms around Hawai'i are driven by seasonal cycles of both light and diazotrophs
- Isopycnal uplift in cyclonic eddies and nearshore upwelling cause short-lived bloom events

Correspondence to:
T. Friedrich,
tobiasf@hawaii.edu

Citation:
Friedrich, T., Powell, B. S., Stock, C. A., Hahn-Woernle, L., Dussin, R., & Curchitser, E. N. (2021). Drivers of phytoplankton blooms in Hawaii: A regional model study. *Journal of Geophysical Research: Oceans*, *126*, e2020JC017069. https://doi.org/10.1029/2020JC017069

Received 14 DEC 2020
Accepted 7 MAY 2021

Abstract The region around the main Hawaiian Islands (MHI) is characterized by a permanent thermocline, and numerous processes have been proposed to facilitate phytoplankton blooms in this oligotrophic province. Here, we use a coupled physical-biogeochemical model of the MHI to elucidate some of the different dynamics behind phytoplankton blooms. The model permits submesoscale processes and is integrated for the years 2010–2017 embedded in a physical state-estimate reanalysis using nearly 50 million observations. Model results exhibit good agreement between simulated values and observations at Station ALOHA for physical and biogeochemical parameters. The overall levels and the amplitude of the seasonal cycles are well captured for many variables. We show that variations in net primary production are mainly driven by domain-wide seasonal cycles of light and nitrogen fixers, respectively, as well as short-lived, stochastic bloom events resulting from the formation of eddies to the west of the island of Hawaii. Furthermore, sporadic wind- and current-driven upwelling is resulting in ephemeral enhancements of nearshore phytoplankton blooms mainly on the northeastern side of the islands.

Plain Language Summary With respect to algae blooms, the region around the main Hawaiian Islands (MHI) is mainly an ocean desert. Here we use a regional marine ecosystem model of the MHI to elucidate different dynamics behind phytoplankton blooms. Model results exhibit good agreement between simulated values and observations. Our results show that algae blooms are mainly controlled by domain-wide seasonal cycles of light and nitrogen fixation respectively. Furthermore, ocean eddies and coastal upwelling can lead to ephemeral nearshore phytoplankton blooms.

1. Introduction

The North Pacific Subtropical Gyre (NPSG) is the largest marine ecosystem on Earth, comprising about 12% of the Pacific Ocean (D. M. Karl & Church, 2017). The main Hawaiian Islands (MHI) are located at the southern edge of the NPSG, and a permanent thermocline inhibits the vertical mixing of nutrients into the euphotic zone severely limiting phytoplankton productivity. The Hawaiian island chain has a significant impact on atmospheric and oceanic circulation and the marine ecosystem in the region. The archipelago is an obstacle to the North Equatorial Current, and the mountains located on the island of Hawaii as well as on Maui disrupt the persistent northeast trade winds, resulting in unique circulation patterns in both the atmosphere and the ocean (Xie et al., 2001). At the mesoscale, the wind stress difference between the typically windswept channel between Maui and the island of Hawaii and the calmer lee of Hawaii leads to the formation of eddies to the west of the MHI (Calil et al., 2008; Chavanne et al., 2002; Jia et al., 2011; Patzert, 1969).

Numerous observation-based and modeling studies have explored the dynamics around the MHI that drive phytoplankton blooms in this oligotrophic environment. Data gathered by the Hawaii Ocean Time-series station program (HOT, D. M. Karl and Lukas, 1996) and Station ALOHA (D. M. Karl & Church, 2018) to the north of Oahu have proven invaluable. Observation-based studies have suggested that phytoplankton blooms around the MHI can result from numerous processes: (1) A deepening of light penetration and hence of the euphotic zone across the nitracline (R. M. Letelier et al., 2004); (2) Sporadic, short-lived nutrient injections through mesoscale and sub-mesoscale processes (Brown et al., 2008; Johnson et al., 2010; Kuwahara et al., 2008; Nencioli et al., 2008; Rii et al., 2008; Vaillancourt et al., 2003); (3) Nitrogen fixation

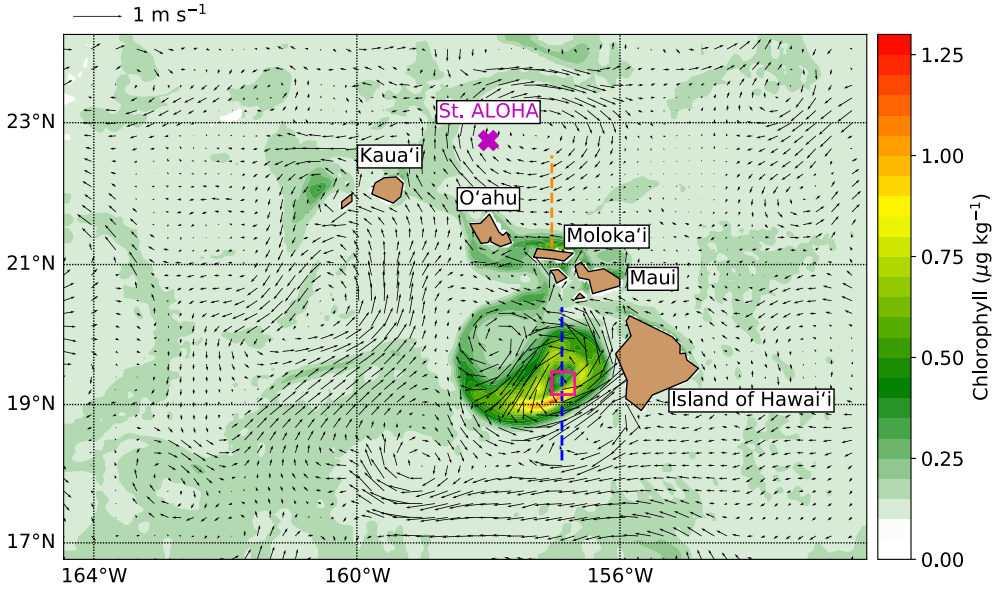

Figure 1. Model domain and snapshot of simulated near-surface chlorophyll (vertically averaged over 0–50 m, μg kg^{-1}) and currents for 3 March 2013. For clarity, only every fifth current vector is drawn. The location of Station ALOHA is indicated by the magenta cross. The dashed vertical lines indicate the meridional sections shown in Figures 10 (blue line) and 13 (orange line). The pink rectangle indicates spatial averaging for model data shown in Figure 11.

(Church et al., 2009; Dore et al., 2002; D. Karl et al., 1997; R. Letelier & Karl, 1996); and (4) Nutrient-rich buoyant plumes caused by lava input (Wilson et al., 2019). Furthermore, an increase in phytoplankton biomass can be observed near the coasts of the islands (Gove et al., 2016).

Numerical studies of the region have so far been limited to one-dimensional biogeochemical models (Fennel et al., 2002; Goebel et al., 2007; Smith et al., 2005) or to physical ocean circulation models (Ascani et al., 2013; Calil et al., 2008; Calil & Richards, 2010). The latter have mainly attempted to explore the role of mesoscale and submesoscale features such as eddies and fronts in displacing isopycnals and inducing vertical transport.

Our present research aims to bridge the gap between mainly local and/or episodic biogeochemical observations and regional model studies of ocean physics by presenting results from a coupled physical-biogeochemical model of the MHI simulating the period 2010–2017. The model permits submesoscale features, and the physical model dynamics are based on a state-estimate reanalysis using nearly 50 million observations (Partridge et al., 2019). This set-up makes the model a unique tool to review hypotheses derived from previous studies and to improve our understanding of processes occurring on spatial and temporal scales not covered by observational data.

We present the model formulation and evaluate the model's performance before examining the drivers of phytoplankton blooms around the MHI.

2. Materials and Methods

To simulate ocean physics and biogeochemistry around the main Hawaiian Islands, we use the Regional Ocean Modeling System (ROMS) coupled to the planktonic ecosystem model Carbon, Ocean Biogeochemistry and Lower Trophics (COBALT).

ROMS is a free surface, hydrostatic, primitive equation model using a stretched coordinate system in the vertical to follow the underwater terrain. ROMS utilizes a split-explicit time stepping scheme to allow different time steps for the barotropic and baroclinic components. More details on ROMS can be found in Shchepetkin and McWilliams (1998, 2003, 2005). Our domain spans the main Hawaiian Islands (Figure 1). The model's bathymetry is based on data provided by the Hawaiian Mapping Research Group (HMRG, 2017).

The grid has 4 km horizontal resolution with 32 vertical s-levels configured to provide a higher vertical resolution in the more variable upper regions. The configuration of the model, including the vertical stretching scheme, is presented in Souza et al. (2015) and Partridge et al. (2019). Tidal forcing is produced using the Oregon State University Tidal Prediction Software (Egbert et al., 1994), which is based on the Laplace tidal equations from TOPEX/Poseidon Global Inverse Solution (TPXO). Tidal constituents included in this simulation are the eight main harmonics; M_2, S_2, N_2, K_2, K_1, O_1, P_1, Q_1, as well as two long period and one non-linear constituent; M_f, M_m, and M_4. The tidal harmonics are updated each year to define the phases referenced to the middle of that year in order to avoid any long term drifting of the tidal amplitudes and phases related to constituents we do not consider.

A sponge layer of 12 grid cells (48 km) linearly relaxes the viscosity by a factor of four and diffusivity by a factor of two close to the boundary to account for imbalances between lateral boundary conditions and ROMS. Lateral boundary conditions and restoring fields for ocean physics are taken from a reanalysis state estimate of the physical ocean state that was derived in a previous study covering the period mid-2007 to mid-2017 (Partridge et al., 2019). This state estimate has the same model grid (4 km horizontal resolution with 32 vertical s-levels) and was produced based on nearly 50 million physical observations using the incremental strong constraint 4D-Variational data assimilation implemented in ROMS (Powell et al., 2008; Moore, Arango, Broquet, Powell, et al., 2011; Moore et al., 2011a, 2011b). Our simulation is running embedded in the assimilated solution of Partridge et al. (2019) using a restoring timescale of 12 days for physical variables to avoid deviation from the state estimate due to the growth of small perturbations.

Atmospheric forcing of ROMS is based on the high-resolution output of a Weather Regional Forecast (WRF) model (Hitzl et al., 2014). WRF provides hourly forcing fields of surface air pressure, surface air temperature, long- and short-wave radiation, relative humidity, rain fall rate, and 10 m wind speeds with 6 km resolution across the entire domain.

The planktonic ecosystem model COBALT (C. A. Stock et al., 2014) uses 33 state variables to resolve global-scale cycles of carbon, nitrogen, phosphorous, iron, and silica. The biomass currency variable in COBALT is nitrogen, which is combined with carbon based on the Redfield ratio of 106:16 (Redfield, 1963). A ratio of 1:40 is applied to the phosphorous-to-nitrogen stoichiometry of the simulated diazotrophs. For all other phytoplankton, zooplankton, and bacterial pools, the Redfield ratio of 1:16 is used. Phytoplankton iron is modeled with a dynamic internal cell quota with iron uptake rates based on ambient iron concentrations and internal quota determined by the rates of iron uptake versus growth (C. A. Stock et al., 2014; Sunda & Huntsman, 1997).

COBALT considers three phytoplankton groups: small, large, and diazotrophs. Primary production by each phytoplankton group is determined by light, nutrient availability, and basal and biosynthetic metabolic costs following Geider et al. (1997). Three zooplankton groups are simulated in COBALT: small (<200 μm), medium (200–2,000 μm), and large (2–20 mm). Nitrogen detritus produced by phytoplankton, zooplankton, and higher predators sinks at a speed of 100 m d^{-1}. Unprotected organic matter is remineralized to e^{-1} of its original concentration after sinking for 188 m. Remineralization can be prevented for a protected fraction of organic material by the presence of biogenic minerals and lithogenic material. Oxygen and carbon are exchanged between the atmosphere and the ocean. Oxygen is produced during photosynthesis and lost during respiratory activities. Total alkalinity (TA) and dissolved inorganic carbon (DIC) serve as tracers for the marine carbon cycle. A comprehensive description of COBALT including details on model dynamics, the governing equations, and parameter settings can be found in C. A. Stock et al. (2014). More details on the coupling, implementation, and performance of ROMS/COBALT can be found in Dussin et al. (2019), Van Oostende et al. (2018), and Zhang et al. (2018).

COBALT is nested within ROMS and is integrated using the same timestep as the physical model. Changes in biogeochemical variables affect the physical ocean model only via chlorophyll-dependent light attenuation (Manizza et al., 2008). In addition to the physical fields, COBALT is forced by lateral boundary conditions and atmospheric CO_2 concentrations. Lateral boundary conditions are derived from a global COBALT simulation (C. A. Stock et al., 2014) covering the period 1988–2007. The output of this global simulation is used to generate monthly climatological fields for all required COBALT variables. Hence, our derived lateral

boundary conditions for COBALT do not account for interannual variability and follow a strictly seasonal cycle.

To account for parametrization differences between the global model and our regional model as well as the difference in time periods covered by both simulations, a bias correction is applied to the vertical profiles of DIC, TA, O_2, silicate, nitrate, and inorganic phosphate at the boundaries of the regional model. Vertical profiles of these variables were derived using monthly measurements provided by the HOT program averaged for the time period of 2010–2017. Then, corresponding profiles were extracted from the fields of the global COBALT simulation at the grid point of Station ALOHA (22.75°N/158°W). The difference between the profiles is determined for each variable, and this bias is then subtracted from the profile at the lateral boundaries of our model domain. It should be noted that using a bias correction based on a single profile over the entire length of the model's boundaries may introduce errors to the domain since it assumes a constant bias across the model domain and cannot account for potential seasonal changes in model-observation differences. This procedure was mainly adopted based on the lack of observational data closer to the boundaries. However, the location of Station ALOHA was chosen to be representative of the greater oligotrophic NPSG habitat (D. M. Karl & Church, 2017) that defines the domain's boundaries. We believe that in the absence of more adequate observational data, our bias-correction procedure is appropriate. As described later in the manuscript, the presence of the Hawaiian Islands creates characteristic regions in which physical-biogeochemical dynamics differ substantially from the ones in the oligotrophic NPSG. Consequently, we chose to only apply bias corrected boundary (and initial) conditions. A restoring of COBALT variables within the model domain is not applied.

Initial conditions for COBALT for 1 January 2010 were created by interpolating the de-biased, climatological fields from the global COBALT simulation onto the regional grid using the month of January. The spinup time of the model for upper-ocean processes that are the focus of our paper was determined to be 6 months.

Atmospheric CO_2 concentrations are prescribed based on weekly data provided by the Mauna Loa Observatory Keeling et al., 1976). Atmospheric O_2 concentrations are assumed to be constant. Atmospheric iron input is set to 7.3 μmol m^{-2} $year^{-1}$ based on an estimate by L. M. Letelier et al. (2019). All other atmospheric or terrestrial input of nutrients is set to zero.

3. Results and Discussion

3.1. Evaluation of Model Results

The physical variables of our model simulation are only weakly affected by the biogeochemical fields and are largely determined by the boundary and restoring conditions taken from the decadal reanalysis conducted by Partridge et al. (2019). In this study, it was shown that modeled Sea Surface Temperature (SST) and Sea Surface Height (SSH) fields exhibit a high pattern correlation with the remotely sensed data used for the data assimilation throughout the decade long simulation (see their Figure 8). Examining our results, we find that nesting within this state estimate provides consistent results with Partridge et al. (2019) (not shown). Thus, we will focus on the validation of the COBALT biogeochemical fields.

The HOT program has obtained physical and biogeochemical observations with approximately monthly resolution since October 1988 and provides an ideal dataset for the evaluation of our model data. Biases, root mean squared errors (RMSE) and correlations for all comparisons of simulated and observed time series and profiles are provided in Table 1. We start by checking the model's performance for capturing parameters that exhibit a clear seasonal cycle. Using a harmonic fit with a periodicity of 1 year and three parameters (A, B, C) of the form

$$f(A,B,C,t) = A + B \cdot sin(2 \cdot \pi \cdot t \,/\, 365) + C \cdot cos(2 \cdot \pi \cdot t \,/\, 365) \quad (1)$$

observed and simulated data, respectively, are decomposed into a mean seasonal cycle and residuals. Subsequently, a linear regression line was subtracted from these residuals for calculating correlations.

The mixed-layer temperature at Station ALOHA is well captured by the simulation (Figures 2a–2c). The mixed layer depth was determined using the temperature criteria of de Boyer Montégut et al., 2004. The

Table 1
Model-Observation Comparison for Station ALOHA (and MODIS) Data: Biases, Root Mean Squared Errors (RMSE) and Correlations

Variable	Bias	RMSE	Correlation	Shown in
Temperature (mixed layer)	0.28 K	0.58 K	0.91	Figure 2a
Oxygen (mixed layer)	−3.90 μmol kg^{-1}	4.94 μmol kg^{-1}	0.68	Figure 2b
pCO_2 (surface)	−2.40 μatm	9.31 μatm	0.83	Figure 2c
MLD	−26.00 m	30.28 m	0.72	Figure 3a
sDIC (surface)	−11.38 μmol kg^{-1}	20.72 μmol kg^{-1}	−0.09	Figure 3b
DIN (surface)	−0.011 μmol kg^{-1}	0.022 μmol kg^{-1}	0.11	Figure 3c
Aragonite				
Saturation (surface)	0.062	0.087	0.68	Figure 3d
Salinity (mixed layer)	0.001 psu	0.14 psu	0.59	Figure 3e
sTA (surface)	−8.57 μmol kg^{-1}	21.79 μmol kg^{-1}	−0.19	Figure 3f
Silicate (surface)	−0.11 μmol kg^{-1}	0.22 μmol kg^{-1}	0.08	Figure 3g
Phosphate (surface)	−0.03 μmol kg^{-1}	0.04 μmol kg^{-1}	0.19	Figure 3h
DIC (profile)	6.17 μmol kg^{-1}	9.93 μmol kg^{-1}	0.99	Figure 4a
TA (profile)	7.23 μmol kg^{-1}	9.70 μmol kg^{-1}	0.99	Figure 4b
Oxygen (profile)	−1.17 μmol kg^{-1}	7.93 μmol kg^{-1}	0.99	Figure 4c
Phosphate (profile)	−0.0026 μmol kg^{-1}	0.075 μmol kg^{-1}	0.99	Figure 4d
Nitrate (profile)	0.24 μmol kg^{-1}	1.06 μmol kg^{-1}	0.99	Figure 4e
Silicate (profile)	0.39 μmol kg^{-1}	2.83 μmol kg^{-1}	0.99	Figure 4f
Surface chlorophyll (domain average)	0.013 μg kg^{-1}	0.018 μg kg^{-1}	0.82	Figure 5a
Surface chlorophyll (compared to HOT)	−0.013 μg kg^{-1}	0.031 μg kg^{-1}	0.41	Figure 5b
Surface chlorophyll (MODIS at St. ALOHA)	−0.001 μg kg^{-1}	0.017 μg kg^{-1}	0.66	Figure 5b
NPP (0–100 m)	22.26 mg C m^{-2} d^{-1}	89.48 mg C m^{-2} d^{-1}	0.38	Figure 5c
Chlorophyll (profile, summer)	−0.011 μg kg^{-1}	0.146 μg kg^{-1}	0.40	Figure 5e
Chlorophyll (profile, winter)	−0.011 μg kg^{-1}	0.144 μg kg^{-1}	0.33	Figure 5e

simulated mixed-layer temperature is 0.28°C warmer than the observation. The correlation amounts to 0.91 with a RMSE of 0.58°C (Table 1). The simulated seasonal amplitude is 7.5% larger. The phases of the observed and simulated seasonal cycles are identical. The detrended residuals (Figure 2c) exhibit a correlation of 0.80 and a standard-deviation ratio of 0.99. This result demonstrates that using a state-estimate reanalysis, the model is capable of representing physical dynamics that go beyond the seasonal cycle. Mixed-layer oxygen concentrations (Figures 2d–2f) are underestimated by 3.90 μmol kg^{-1} (~2.0%) of which the slightly warmer simulated mixed-layer temperature can explain ~1 μmol kg^{-1} due to the reduced oxygen saturation. The RMSE and correlation for mixed layer oxygen amount to 4.94 μmol kg^{-1} and 0.68, respectively (Table 1). Simulated mixed-layer oxygen exhibits a phase lag of 1 month compared to the observations. The seasonal oxygen amplitude is overestimated by 24% in the model. One possible contribution to this discrepancy can be found in the fact that simulated mixed layer depth is shallower than the observed one (Figure 3a). It should be noted, however, that scarcity of observational data may have an effect on the phase and amplitude of the harmonic fit. The correlation between the detrended mixed-layer oxygen residuals (Figure 2f) amounts to 0.57, and the ratio of the standard deviations is 0.98. Simulated surface pCO_2 is lower by 2.40 μatm and precedes the observed seasonal cycle by half a month (Figures 2g–2i). The simulated pCO_2 amplitude is 48% larger, and the shallower-than-observed mixed layer depth likely contributes to this overestimation. The correlation of the detrended residuals is 0.28, and the standard deviation ratio is 1.09.

Observed salinity-normalized DIC (sDIC) at Station ALOHA for the years 1988–2002 was found to exhibit a seasonal cycle with a minimum around October followed by a fall and wintertime increase (Keeling

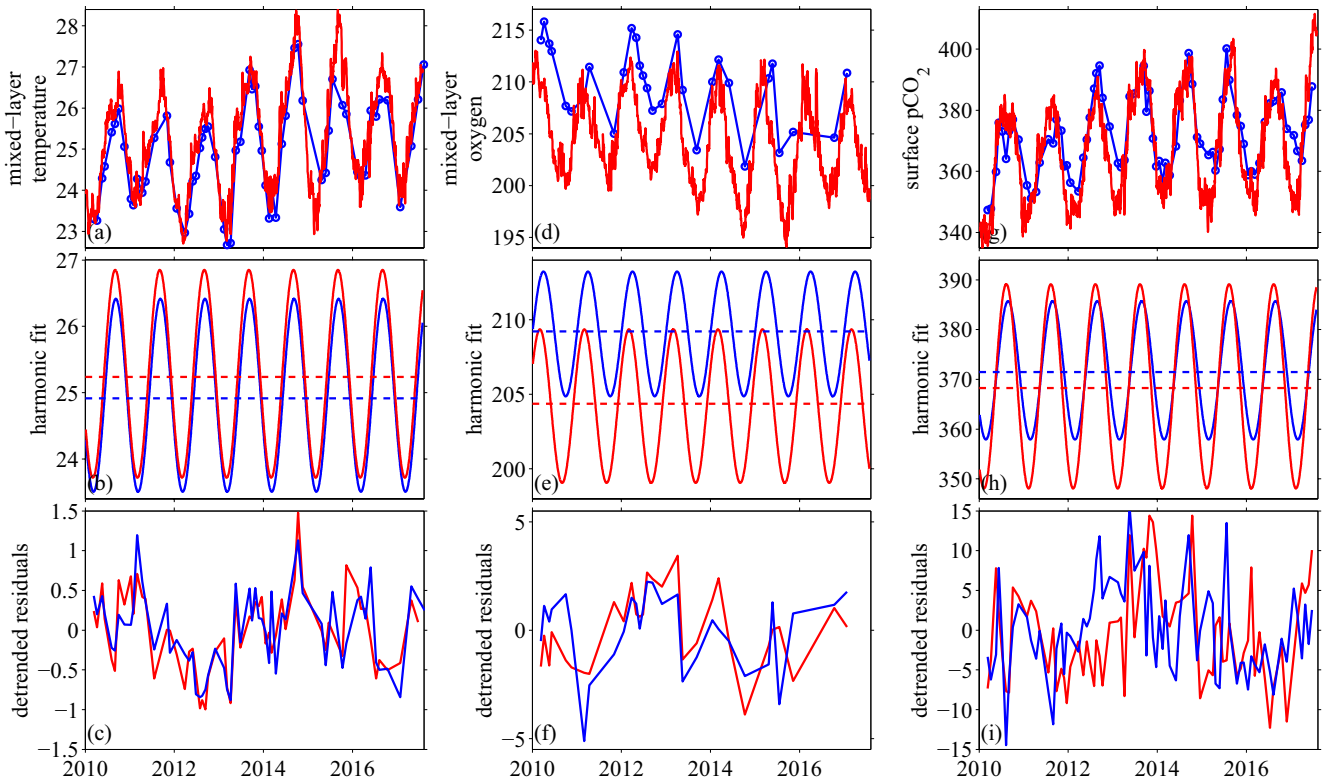

Figure 2. Evaluation of model data: time-series of mixed-layer and surface parameters. Comparison of simulated (red) and observed (blue) parameters at Station ALOHA. (a) mixed-layer temperature (°C); (b) Harmonic fit of mixed-layer temperature. Dashed lines indicate mean values; (c) Detrended residuals of mixed-layer temperature. (d)–(f) as in (a)–(c) for mixed-layer oxygen (μmol kg^{-1}). (g)–(i) as in (a)–(c) for surface partial pressure of CO_2 (pCO_2, μatm). Mixed layer depth was determined using the temperature criteria of de Boyer Montégut et al. (2004). See also Figure 3.

et al., 2004). A similar, however less pronounced, cycle can also be identified for the years 2010–2017 (Figure 3b). Simulated sDIC shows a fall and wintertime rise for the years 2012–2014 but is subject to a larger short-term variability than observed sDIC. The mean values of simulated and observed sDIC agree well with a model bias of −11.38 μmol kg^{-1} (Table 1). A seasonal cycle cannot be identified for surface sTA at Station ALOHA–neither in the observations nor in the model data (Figure 3f). Simulated sTA exhibits larger short-term fluctuations than the observations. The model bias with respect to the temporal mean amounts to −8.57 μmol kg^{-1}.

Simulated surface nitrate concentrations at Station ALOHA location are near zero and persistently smaller than observed values (not shown). Almost all the simulated dissolved inorganic nitrogen (DIN) near the surface is in the form of ammonia, presumably due to slow nitrification. Modeled growth of small and large phytoplankton, however, is mainly determined by the total available nitrogen. The *in-situ* snapshot observations of nitrate and nitrite at Station ALOHA exhibit a high variability on the timescale of days (Figure 3c) that is not seen for the simulated DIN. It should be noted that despite the use of a physical state estimate and realistic forcing for our simulation, model-observation covariance for these short-term (day-to-day) fluctuations cannot be expected. The mean values of observed nitrate and nitrite and simulated DIN are in acceptable agreement with a model bias of −0.011 μmol kg^{-1}.

The simulated surface aragonite saturation is in good agreement with the observations (Figure 3d and Table 1). A late summer/fall maximum is visible in both modeled and observed data but tends to be slightly overestimated in the simulation.

Simulated mixed-layer salinity (Figure 3e) has a different variability (likely due to the rain and evaporation data provided by WRF) but the observed and overall downward trend toward the end of the simulation that is visible in the observations is well captured by the modeled salinity. Simulated surface silicate exhibits a smaller variability compared to observations (Figure 3g). However, the mean concentrations are in good

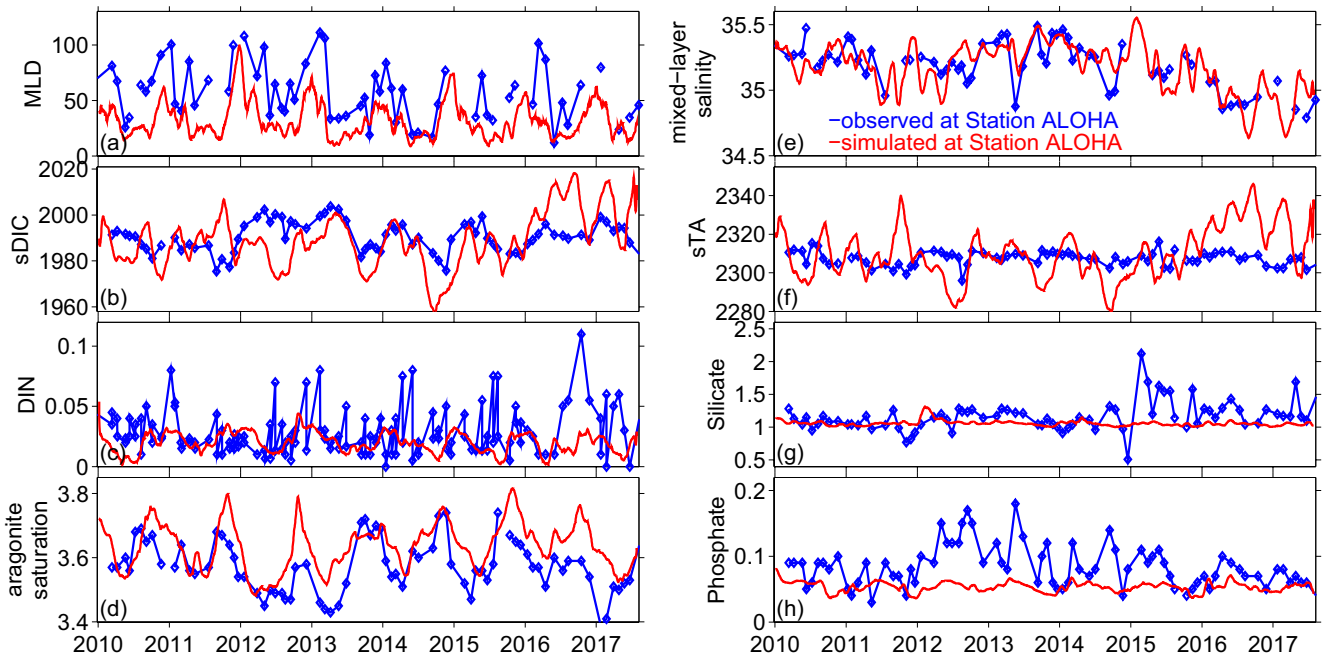

Figure 3. Evaluation of model data: time-series of mixed-layer and surface parameters. Comparison of simulated (red) and observed (blue) parameters at Station ALOHA. (a) Mixed layer depth (m); (b) salinity-normalized, surface dissolved inorganic carbon (sDIC, μmol kg^{-1}); (c) surface dissolved inorganic nitrogen (DIN, μmol kg^{-1}), modeled: sum of inorganic nitrate and ammonia, observations: sum of nitrate and nitrite; (d) surface aragonite saturation; (e) mixed-layer salinity (psu); (f) salinity-normalized, surface total alkalinity (sTA, μmol kg^{-1}); (g) surface silicate (μmol kg^{-1}); and (h) surface inorganic phosphate (μmol kg^{-1}). Simulated data are based on daily averages smoothed by using a running window of 30 days. Simulated data was vertically averaged over the first 5 s-levels (0–17 m).

agreement. The temporal evolution of observed surface phosphate differs substantially from the simulated concentration (Figure 3h). While the simulated and observed magnitudes agree well during periods of low phosphate concentrations, the period of 2012–2014 is characterized by relatively high observed phosphate at Station ALOHA that is not captured by the model. Recent research by L. M. Letelier et al. (2019) showed that oscillations in phosphate can be explained by changes in the North Pacific Oscillation altering the sea-level pressure in the Northwest Pacific and the deposition of iron dust from Asia. This cycle of deposition determines periods of either iron or phosphate limitation. During the iron limitation phase, phosphate is abundant. Resolving this process would require interannually varying boundary conditions and employing a model of atmospheric dust transport that could not be incorporated for this experiment.

Observed, time-averaged profiles of DIC, TA, O_2, phosphate, nitrate, and silicate at Station ALOHA are well captured by the simulation (Figure 4). All profile correlations amount to 0.99, and the simulated RMSEs surface concentrations of simulated and observed nitrate and phosphate are near zero. The vertical increase in modeled nutrient concentrations starts at slightly shallower depths than for observed nitrate and phosphate. O_2 concentrations are overestimated by the model in the depth levels of minimum concentrations (600–1,000 m, Figure 4c), whereas DIC, nitrate, and phosphate are underestimated at this depth. This pattern of differences in the vertical profile is indicative of remineralization of organic matter occurring at shallower levels in the model compared to the observations. In addition, the model's vertical resolution in this depth range around Station ALOHA is in the order of 100–200 m which leads to a smoothing of vertical gradients. It must be noted that using bias-corrected boundary and initial conditions contributes to the good agreement between simulated and observed profiles. However, after the start of the simulation, the bias correction is only applied at the open boundaries. The good agreement between observed and modeled profiles provides evidence that the dynamics of the processes are captured by the model with consistent parametrization of the model's physics and biogeochemistry.

Estimates provided by the Moderate Resolution Imaging Spectroradiometer (MODIS, NASA Goddard Space Flight Center et al., 2018) allow for a domain-wide comparison between remotely sensed and modeled

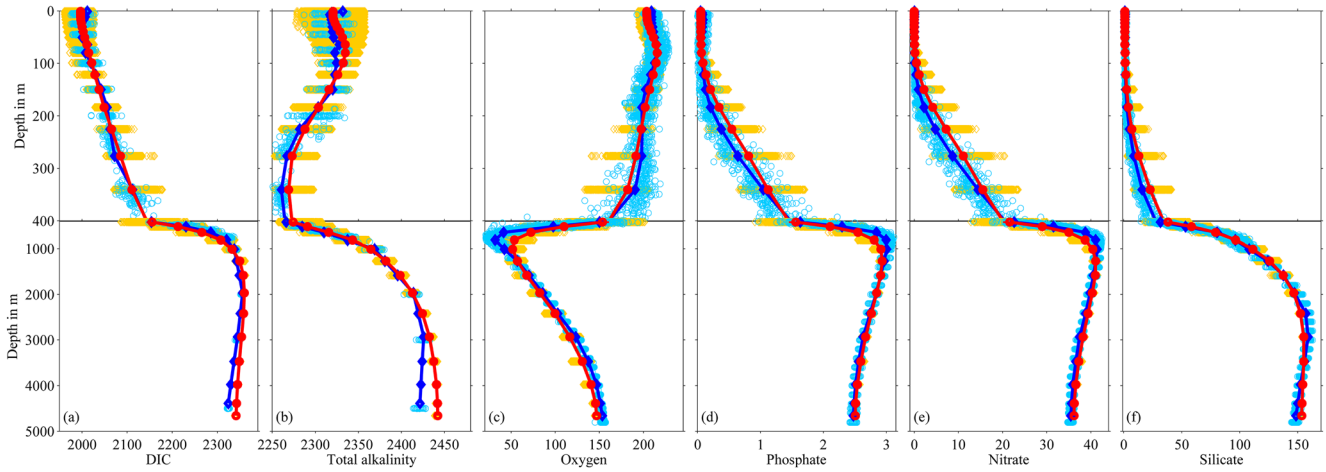

Figure 4. Evaluation of model data: vertical profiles. Comparison of simulated (red, orange) and observed (blue, cyan) profiles at Station ALOHA. (a) dissolved inorganic carbon (DIC); (b) alkalinity; (c) oxygen; (d) phosphate; (e) nitrate (The sum of nitrate and nitrite is shown for Station ALOHA data.); and (f) silicate. All data are in μmol kg^{-1}. Blue and red line show time-averaged data. Time-averages for HOT data were interpolated to the model's depth axis at the Station ALOHA location to allow for better comparison. Orange and cyan dots indicate individual measurements (observations) and daily values (model). Please note the split *y*-axis.

surface chlorophyll data (Figure 5a). The seasonality of surface chlorophyll—with higher concentrations during the winter half—is well captured by the model. Higher simulated chlorophyll can partly be attributed to the fact that MODIS reports *chlorophyll a* concentrations whereas modeled chlorophyll represents a sum. Chlorophyll profiles at Station ALOHA show that *chlorophyll b* concentrations can reach about one quarter to one third of *chlorophyll a* levels. However, the contribution by *chlorophyll b* tends to be smaller in the upper water column. Hence, it is likely that the model slightly overestimates total surface chlorophyll concentrations.

Near-surface chlorophyll concentrations are in good agreement for modeled, remotely sensed and *in situ* observations at Station ALOHA (Figure 5b). The time-averaged vertical profiles of chlorophyll exhibit a deep chlorophyll maximum layer (DCML) in the observed and in the simulated data (Figure 5e). A deepening of the DCML during the summer months (L. M. Letelier et al., 2004) is captured by the model. However, the simulated summer DCML occurs approximately 20 m—on average—shallower than the observed one. For winter time, the discrepancy is even higher, reaching ~35 m. The exact reason for this mismatch is unclear. We speculate that the parameterization of the dynamical chlorophyll-to-carbon ratio (Geider et al., 1997) and the vertical model resolution of ~20 m at this location and depth range contribute to the shallower simulated DCML. Furthermore, the representation of low-versus high-light adapted phytoplankton cells (Thompson et al., 2021) needs to be enhanced. Improving the representation of the DCML will therefore be the goal of future fine-tuning of the model.

Estimates of daytime net primary production (NPP) integrated over the upper 100 m are in the order of 400–800 mg C m^{-2} d^{-1} for the Station ALOHA location (Figure 5c). This range is well represented by our model results. It should be noted that—by default—the COBALT model outputs NPP integrated over the upper 100 m and ignores productivity below. However, observational data from Station ALOHA indicate that only 11.6 ± 6% of NPP is occurring below 100 m underscoring the validity of our comparison. Daily values of simulated (daytime) NPP exhibit large short-term fluctuations associated with changes in shortwave radiation and mesoscale features that are not seen in the monthly observation-based estimates.

Concentrations of mesozooplankton (>200 μm) in the upper 150 m were reported to be in the range of 0.19–0.28 mmol C m^{-3} at Station ALOHA for the time period 1994–1997 (C. Stock & Dunne, 2010; Roman et al., 2001). Averaging the sum of the simulated medium and large zooplankton classes (>200 μm) over the upper 150 m, it can be seen that the modeled range amounts to ~0.15–0.40 mmol C m^{-3} with a mean of 0.28 mmol C m^{-3} (Figure 5d).

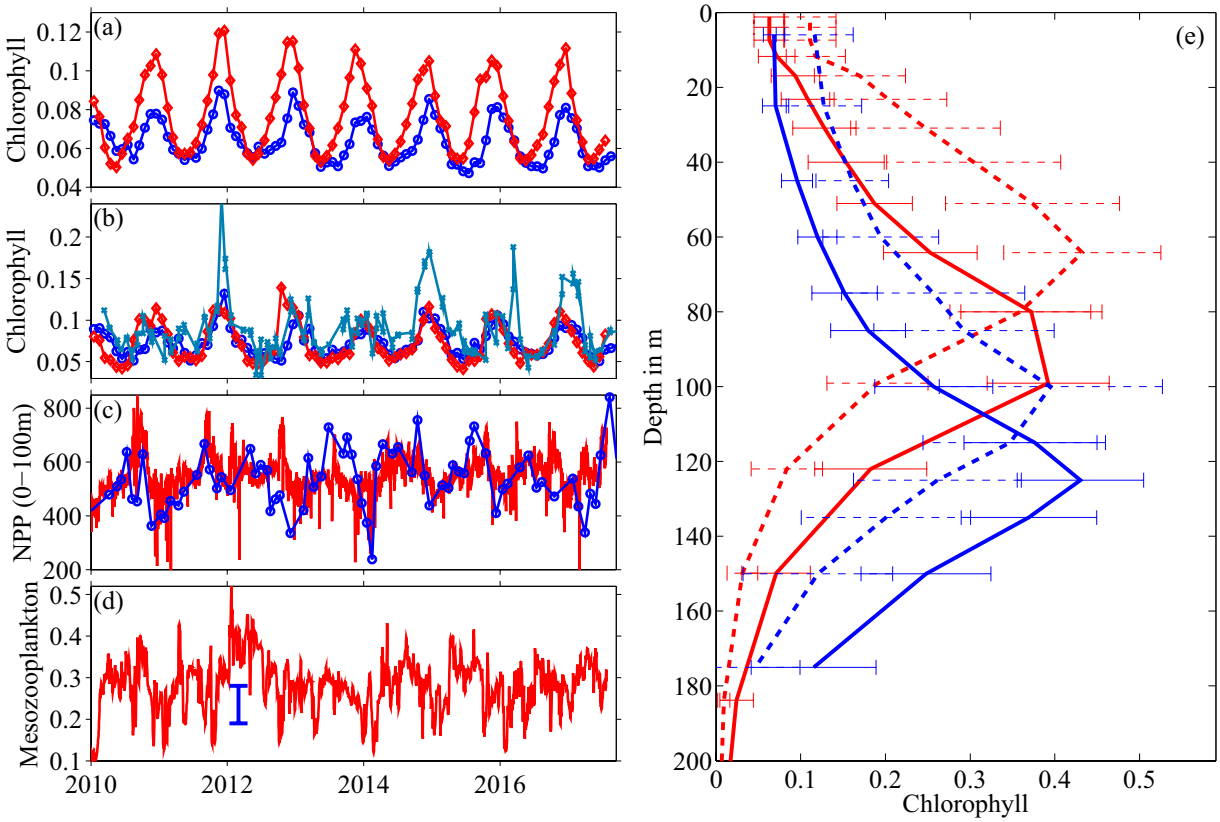

Figure 5. Model-observation comparison for remotely sensed and *in situ* chlorophyll, net primary production and zooplankton. (a) Spatially averaged monthly mean near-surface simulated (red) and remotely sensed (blue) chlorophyll concentrations. (b) As in (a) for Station ALOHA with cyan line representing *in situ* chlorophyll data. (c) Comparison of daytime net primary production (NPP, mg C m^{-2} d^{-1}) integrated over the upper 100 m observed (blue) and simulated (red) for Station ALOHA. (d) Vertically averaged (0–150 m) mesozooplankton (>200 μm) simulated at Station ALOHA (red, mmol C m^{-3}). The blue bar indicates the range of observed values (C. Stock & Dunne, 2010; Roman et al., 2001). (e) Vertical profiles of chlorophyll concentrations at Station ALOHA of simulated (red) and *in situ* (blue) data. Solid lines indicate temporal averages over summer months; dashed lines over winter months. Horizontal bars indicate standard deviations. All chlorophyll concentrations are given in μg kg^{-1}.

The HOT program is serving physical and biogeochemical data on an approximately monthly basis. As a consequence of the monthly resolution, the temporal evolution and dynamics of processes occurring on timescales shorter than 60 days cannot be captured. ROMS/COBALT on the other hand can output "station data" for designated locations at any given time interval.

Using a Fourier transformation (Baron de Fourier, 1822; Cooley & Tukey, 1965), we decomposed the observed and simulated Station ALOHA oxygen time series (taken at a depth of 420 m) into their frequency components and calculated the corresponding spectral density, which is a measure of the variance contributed to the time series by each frequency. Oxygen was chosen based on the fact that its concentration is affected by ocean physics and biogeochemical processes and therefore typically subject to high temporal variability. The spectra for simulated and observed oxygen at Station ALOHA are in good agreement showing the most energy on annual timescales (Figure 6). However, there is also significant energy associated with timescales shorter than what is resolved by HOT. Writing model data for the Station ALOHA location every 20 min, it can be seen that the spectral energy related to the effect of tides and the diurnal cycle is close to that associated with annual timescales. For those shorter term processes, the model can work as a unique tool to complement observational data and to help understand biogeochemical dynamics occurring on timescales of days to months.

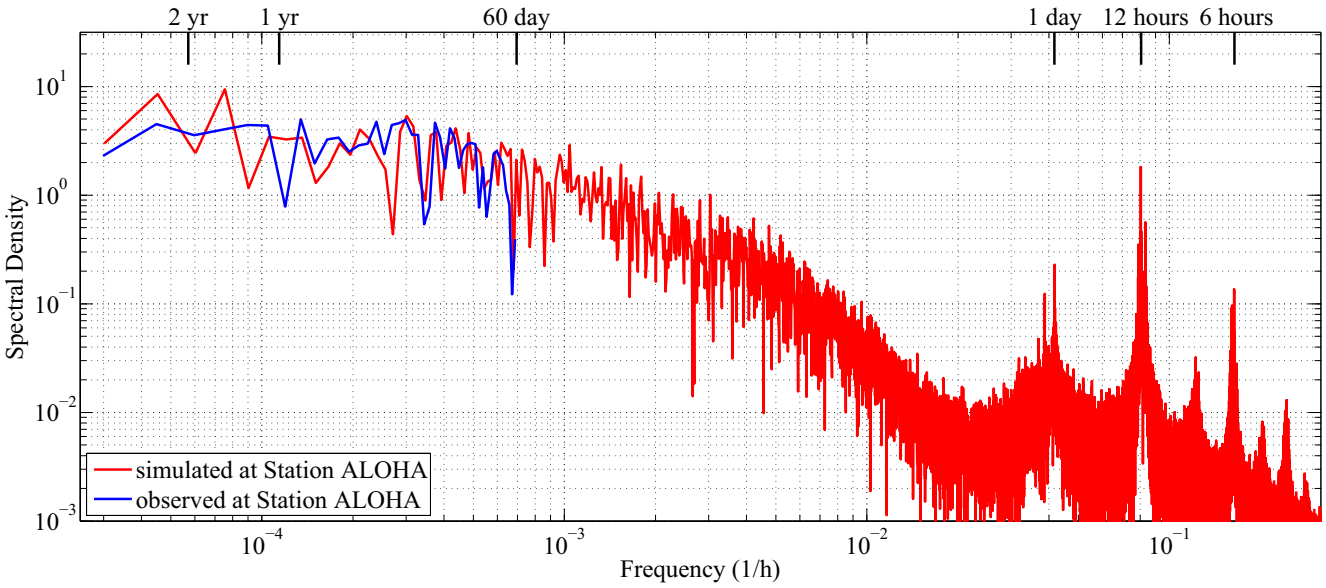

Figure 6. Power spectrum for simulated and observed oxygen at Station ALOHA. Spectral density (μmol kg^{-1} h) for simulated oxygen sampled every 20 min (red) and oxygen observed at Station ALOHA (blue, years 2010–2017). Power spectrum was calculated for oxygen concentrations at a depth of 420 m.

3.2. Drivers of Phytoplankton Blooms

The oceanographic setting of the MHI creates a unique environment when it comes to the dynamics that drive phytoplankton blooms and primary productivity. To the north and to the east of the islands, the permanent thermocline of the NPSG severely limits the vertical entrainment of nutrients into the euphotic zone. In the lee of the islands, the interaction of trade winds, the tall mountains and ocean currents result in mesoscale and sub-mesoscale features that can strongly affect the nutrient availability in the near-surface waters. Furthermore, the water masses are separate. The regions to the north and the east of the islands are dominated by NPSG waters, while to the west of the MHI warmer waters are entrained by the North Equatorial Counter Current (Xie et al., 2001). In the following, we will disentangle the role of these different processes in spurring phytoplankton blooms.

We start by examining the modes of variability of simulated net primary productivity (NPP, integrated over the upper 0–100 m). When calculating the empirical orthogonal functions (EOF), a 12 grid points wide area at the boundaries of the model domain and the first 6 months of the simulation were excluded to avoid biases due to boundary restoring and trends during the spin-up period, respectively. The first three EOFs of NPP explain ~56% of the total variability (Figures 7a–7c) with the first EOF alone accounting for ~41%. The EOF1 exhibits a domain-wide monopole structure (Figure 7a) and a clear seasonal cycle in its principal component (PC1). The PC1 starts to increase early each year and peaks in mid to late summer (Figure 7d). The patterns of the EOF2 and EOF3 show a pronounced minimum/maximum to the west of the island of Hawaii as well as to the north of Molokai and Maui (Figures 7b and 7c). The PC2 and PC3 appear to have a sporadic behavior with spikes that last for time periods of days to weeks.

Simulated small phytoplankton dominates the oligotrophic region (Figure 7f) in good agreement with observations (Campbell & Vaulot, 1993; L. M. Letelier et al., 1993; Partensky & Garczarek, 2010). In the domain average, small phytoplankton contains 49.2 ± 1.2% to the total phytoplankton biomass (averaged for 0–200 m). Large phytoplankton and diazotrophs contribute 36.9 ± 1.0% and 13.9 ± 1.6%, respectively. During net primary production, nitrogen is accumulated in one, two, or all of the three phytoplankton classes represented in COBALT. Spatial averages of the nitrogen content in phytoplankton (Figures 7e–7h) reveal that the temporal evolution of the PC1 can mainly be regarded as a superposition of the seasonal cycles of small phytoplankton and diazotrophs with a smaller contribution by large phytoplankton. The contribution by small phytoplankton to the seasonal NPP maxima stems mainly from an early summer deepening of its vertical extent in the water column. Simulated diazotrophs, on the other hand, are subject

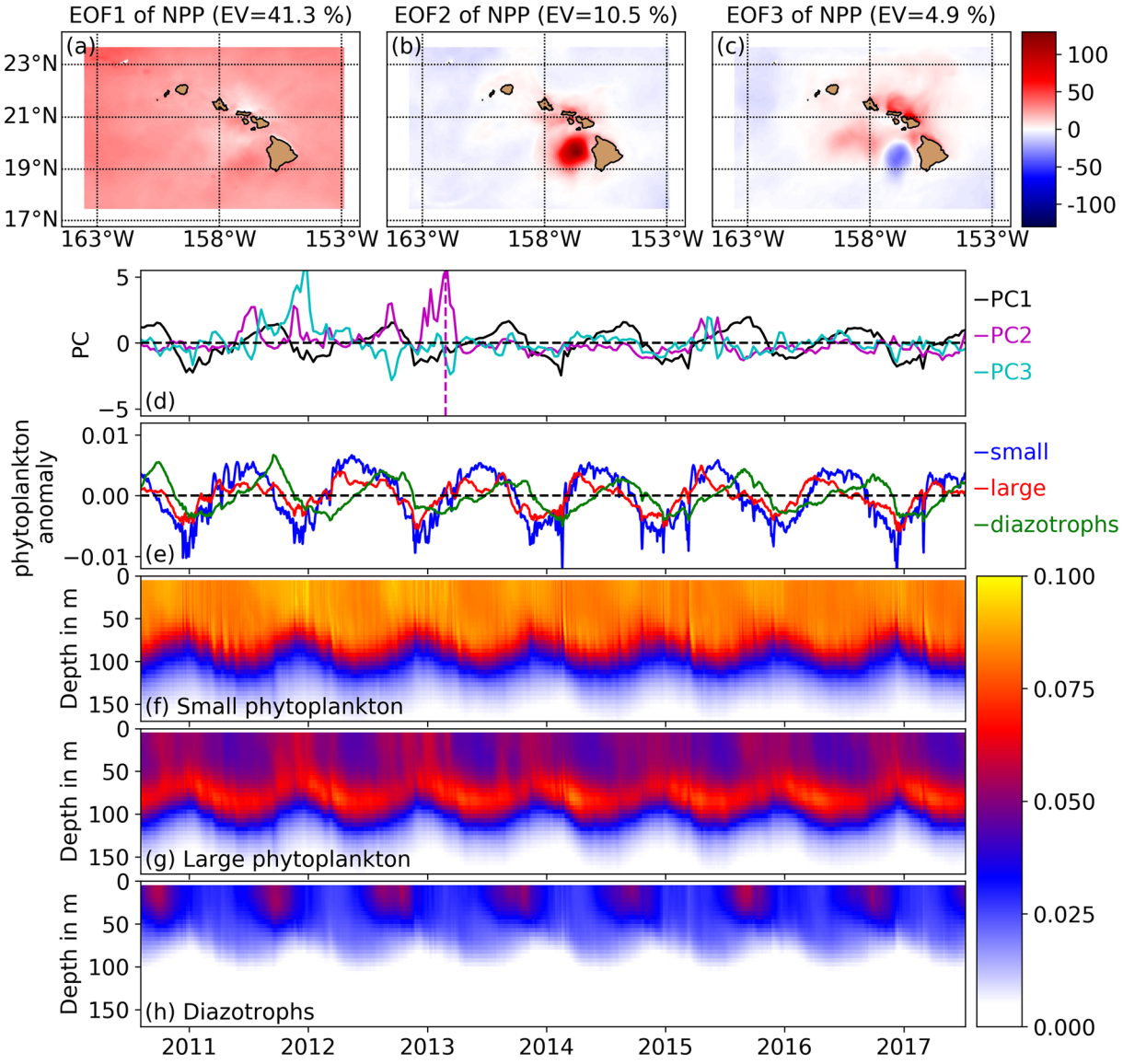

Figure 7. EOF of net primary production (NPP) and domain-averaged phytoplankton concentrations. Panel (a) EOF1 of depth-integrated (0–100 m) NPP (mg C m^{-2} d^{-1}). Panels (b) and (c) as in (a) for EOF2 and EOF3, respectively. Explained variances (EV) are given in the panel titles. A 12 grid points wide area at the boundaries of the model domain as well as the first 6 months of the simulation were excluded from the EOF calculation to avoid biases due to boundary restoring and spin-up trends, respectively. Panel (d) Corresponding PC1 (black), PC2 (magenta), and PC3 (cyan) (no units). Vertical line indicates time of snapshot shown in Figure 1 and time of meridional section shown in Figure 10. (e) domain- and depth-averaged (0–150 m) phytoplankton concentrations for small (blue) and large (red) phytoplankton classes and diazotrophs (green). Panels (f)–(h) Domain-averaged phytoplankton concentrations for the three different classes as indicated in the panels. All phytoplankton concentrations are given in μmol N kg^{-1}.

to shallow, late-summer blooms (Figure 7h) when the vertical extent of small phytoplankton is decreasing. The seasonal amplitude of nitrogen biomass found in large phytoplankton is lower compared to the small class (Figures 7e and 7g). They are also subject to an early summer bloom at depths between 50 and 100 m. However, at the same time concentration of large phytoplankton decrease in the upper water column.

Elucidating the dynamics behind the EOF1 of NPP requires two separate mechanisms that operate on a domain-scale but with a slight seasonal offset. Seasonal changes in solar radiation are an obvious candidate for controlling seasonal changes in NPP on a domain scale and have been identified by L. M. Letelier et al. (2004) as a major driver of early summertime deepening of the DCML and an associated chlorophyll increase in deeper layers of the euphotic zone at Station ALOHA. Figure 8 depicts the seasonal cycle of domain-averaged simulated chlorophyll, nitrate, and irradiance for the upper 150 m. For clarity, only the years

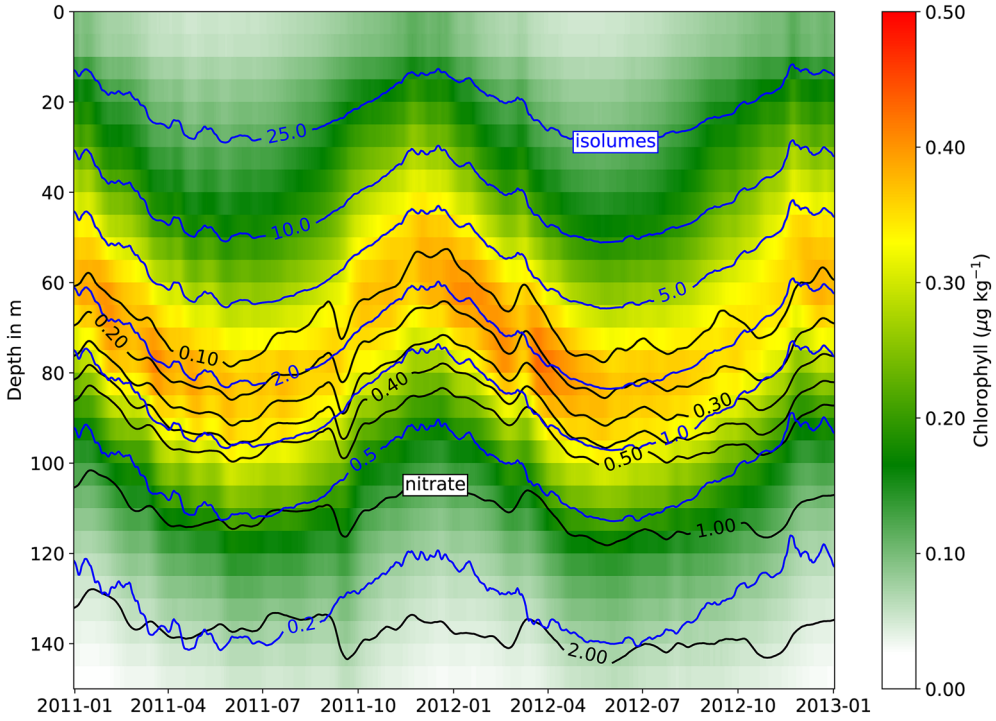

Figure 8. Seasonal cycle of domain-averaged irradiance, chlorophyll, and nitrate concentrations. Domain-averaged chlorophyll (μg kg^{-1}, shaded), irradiance (W m^{-2}, blue lines), and nitrate (μmol kg^{-1}, black lines) for years 2011–2012. Data have been smoothed using a running window with a length of 11 days. Only 2 years are shown for clarity.

2011 and 2012 are shown as examples, but other years exhibit the same evolution. With the overall increase in irradiance at the beginning of the year, the isolumes start to deepen. The difference in simulated isolume depth between summer and winter solstice can reach up to 20 m. As a consequence of this seasonal isolume displacement, the vertical extent of the euphotic zone reaches depths of higher nitrate concentrations. The winter position of the 2 W m^{-2} isolume at the start of year 2011 is at ~60 m and has a corresponding nitrate concentration of 0.1 μmol kg^{-1}. By March 2011, this isolume has deepened to ~77 m and overlaps with a nitrate concentration of almost 0.2 μmol kg^{-1}. The maximum depth of the 2 W m^{-2} isolume of ~83 m at the end of June corresponds to the winter position of the 0.4 μmol kg^{-1} nitrate isoline, which would equate to a quadruplication of the winter nitrate concentration at this isolume. However, the actual nitrate concentrations only reach ~0.15 μmol kg^{-1} since the additional nitrate available to phytoplankton is immediately consumed and removed from the water column.

The position of the simulated DCML follows the displacement of the isolumes. Small phytoplankton contributes the most to the change in simulated chlorophyll with an additional contribution by large phytoplankton at deeper layers; whereas, diazotrophs play only a minor role in this early summer bloom (see also Figures 7f–7h). The simulated domain-scale temporal behavior of isolumes and chlorophyll is in good agreement with the findings by L. M. Letelier et al. (2004) albeit a slightly shallower DCML in the model and our results demonstrate that light-driven dynamics identified at Station ALOHA can be regarded as representing a key mechanism controlling the domain-wide, seasonal chlorophyll concentrations around the MHI.

The seasonal cycle of simulated diazotrophs is mainly determined by irradiance, water column stratification, and excess phosphate concentration. Diazotrophs are modeled according to Trichodesmium in COBALT (Capone et al., 1997; C. A. Stock et al., 2014). Their growth (and nitrogen fixation) strongly depends on the availability of light energy, phosphate, and iron and is inhibited by oxygen (see Equation 7 in Supplementary Material of C. A. Stock et al., 2014). Consequently, their blooms occur in the upper water column during maximum summer SSTs (Figure 9). The summer leads to a strong stratification and a minimum in mixed

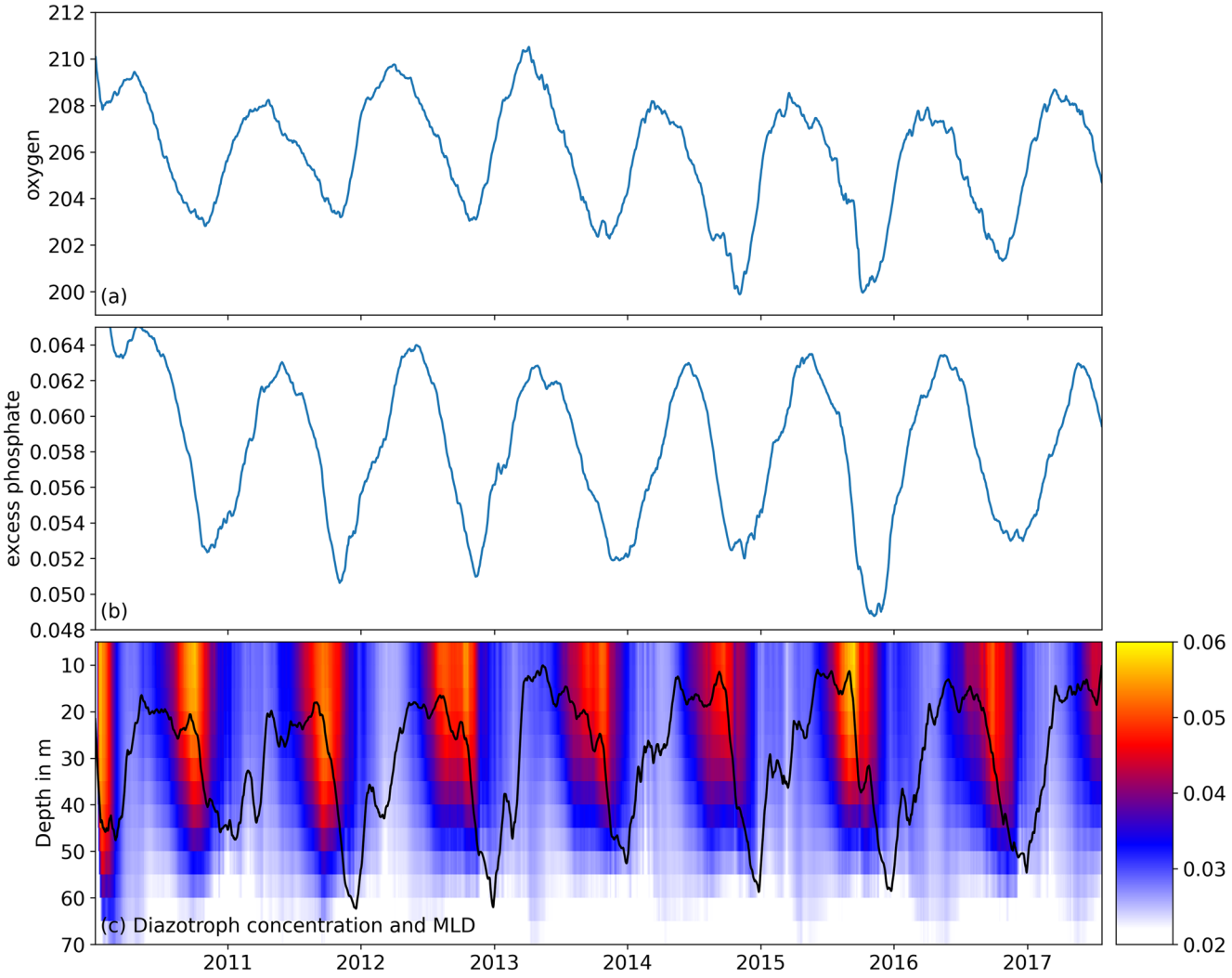

Figure 9. Variables affecting the seasonal cycle of simulated diazotroph concentrations. Panel (a) Domain-averaged, near-surface oxygen concentrations (0–50 m, μmol kg^{-1}). Panel (b) Domain-averaged, near-surface excess phosphate concentrations (0–50 m, μmol kg^{-1}). Please see text and Equation 2 for details. Panel (c) Domain-averaged diazotroph concentration (μmolN kg^{-1}) and mixed layer depth (m). Mixed layer data have been smoothed using a running window with a length of 30 days for clarity.

layer depth (Figure 9c) supplying diazotrophs' need to remain near the well-lit surface. Furthermore, warm SSTs lower oxygen solubility and decrease oxygen inhibition of simulated nitrogen fixation (Figure 9a).

Defining an excess phosphate concentration (PO4*) by comparing the concentrations of nitrate and ammonia in the upper 50 m to the availability of phosphate (scaled by the Redfield ratio):

$$PO4^{*} = (NO3 + NH4) / 16 \quad (2)$$

We also find that the start of the simulated seasonal diazotroph bloom coincides with the seasonal maximum of excess phosphate (Figure 9b). Over the course of the diazotroph bloom, the excess phosphate is consumed resulting in a seasonal minimum of PO4* around the end of each year.

The depth, phase, and amplitude of our regional seasonal cycle of diazotroph blooms are in good agreement with a one-dimensional modeling approach carried out at the Station ALOHA location (Fennel et al., 2002). Our late-summer maximum of diazotroph concentrations are in the order of 0.05–0.15 μmol N kg^{-1} for the Station ALOHA location (based on daily averages). These values compare well with concentrations of 0.05–0.08 μmol N kg^{-1} simulated by Fennel et al., 2002) and with observed values of ~0.065 μmol N kg^{-1}

reported by R. Letelier and Karl 1996) (See conversion between biomass and nitrogen content in Fennel et al., 2002.) The results of our simulation (as well as the ones presented by Fennel et al. (2002)) with respect to diazotrophs are also in good agreement with measurements of nitrogen isotopic ratios and the abundance of the photosynthetic pigment phycoerythrin carried out at Station ALOHA (Dore et al., 2002). However, the maximum of our domain-averaged diazotroph bloom occurs slightly later than what has been observed for Station ALOHA. Simulated nitrogen fixation rates vary from a minimum of 38.6 mmol N m^{-2} $year^{-1}$ in year 2013 to a maximum of 71.5 mmol N m^{-2} $year^{-1}$ in 2016. These values are in good agreement with modeled values presented by Fennel et al. (2002) as well as observations (Church et al., 2009; D. Karl et al., 1997) as shown in Table 2. The drivers of interannual changes in observed, and simulated N_2 fixation rates will be the focus of a future study.

The EOF2+3 and PC2+3 of NPP clearly point to sporadic and short-lived spikes occurring mainly to the west of the island of Hawaii as well as close to islands' coastal areas (Figures 7b–7d). The near-surface chlorophyll and currents associated with the maximum of the PC2 in early 2013 (vertical line in Figure 7d) indicate that cyclonic eddies contribute substantially to these spikes in NPP in this region (Figure 1). The depicted eddy was formed in early February 2013 at the northwestern tip of the island of Hawaii. At the end of March, the eddy propagated westward and lasted as an individual feature until early May when it merged with another cyclonic eddy south of Oahu and eventually dissipated in early July 2013 (not shown). Figure 10 shows key parameters of the eddy for 2 March 2013 along a meridional section indicated by the blue vertical line in Figure 1. The zonal location of the section was chosen based on the near-surface chlorophyll maximum. The SSH exhibits a depression of ~30 cm near the center of the section compared to the edges of the eddy (Figure 10a). Near-surface current velocities increase on either side of the center and reach a maximum of 0.8 m s^{-1} at about 50 km to the north and south of the center before decreasing again (Figure 10a). Based on these physical parameters, the overall meridional extent of the eddy can be approximated by almost ~200 km.

The downward displacement of the sea surface has to be compensated by a doming of the isopycnals in a quasi-geostrophic balance. It can be seen that this doming reaches more than 150 m. The 24.5 kg m^{-3} isopycnal is found at a depth of ~170 m at the eddy's edges but is subject to outcropping near its center (Figure 10b). Consequently, nitrate concentrations increase in the upper euphotic zone by 1–2 orders of magnitude compared to surrounding waters reaching values of up to 10 μmol kg^{-1} (Figure 10b). This injection of nitrate results in a strong but localized increase in simulated productivity in both the small and large phytoplankton class (Figures 10c–10e). The modeled eddy shares several similarities with the cyclonic eddy *Opal* and the simulated dynamics are in very good agreement with observations collected for this eddy (Brown et al., 2008; Nencioli et al., 2008; Rii et al., 2008). *Opal* occurred in February and March of 2005 also to the west of the island of Hawaii and had a similar diameter of ~200 km. The 24.0 kg m^{-3} isopycnal was lifted by more than ~100 m and nitrate concentrations in the euphotic zone increased by 1–2.5 μmol kg^{-1} compared to casts taken outside the influence of the eddy (Nencioli et al., 2008). Furthermore, Brown et al. (2008) reported a strong diatom bloom within the core region of *Opal*, which is consistent with the simulated increase in the large phytoplankton class (Figure 10e).

The overall dynamics of enhanced nutrient supply to the euphotic zone by doming of isopycnals remain active through the lifetime of the simulated eddy but become weaker as the angular velocity of the eddy decreases. NPP near the center of the eddy is about one order of magnitude higher compared to surrounding waters during the early phases and reaches maximum values of ~2,000 mg C m^{-2} d^{-1}. Over the lifetime, the eddy's maximum NPP is reduced to ~500 mg C m^{-2} d^{-1}.

The number of cyclonic eddies forming in the west of the island of Hawaii in our physical state estimate is on average 4.1 per year with a range of 2 (year 2015) to 6 (year 2012) eddies per year. All of these eddies result in a substantial—but localized and relatively short-lived—increase of NPP, underscoring the pivotal role of interactions between Northeast trade winds and the mountains of the western Hawaiian islands for plankton blooms in this oligotrophic region.

Ship-based measurements of eddies are typically limited to a number of transects for one event (e.g., Nencioli et al., 2008). The model provides us with an opportunity to draw a more continuous picture of the (simulated) ecosystem dynamics over a longer period of time. The evolution of eddy-driven changes of the

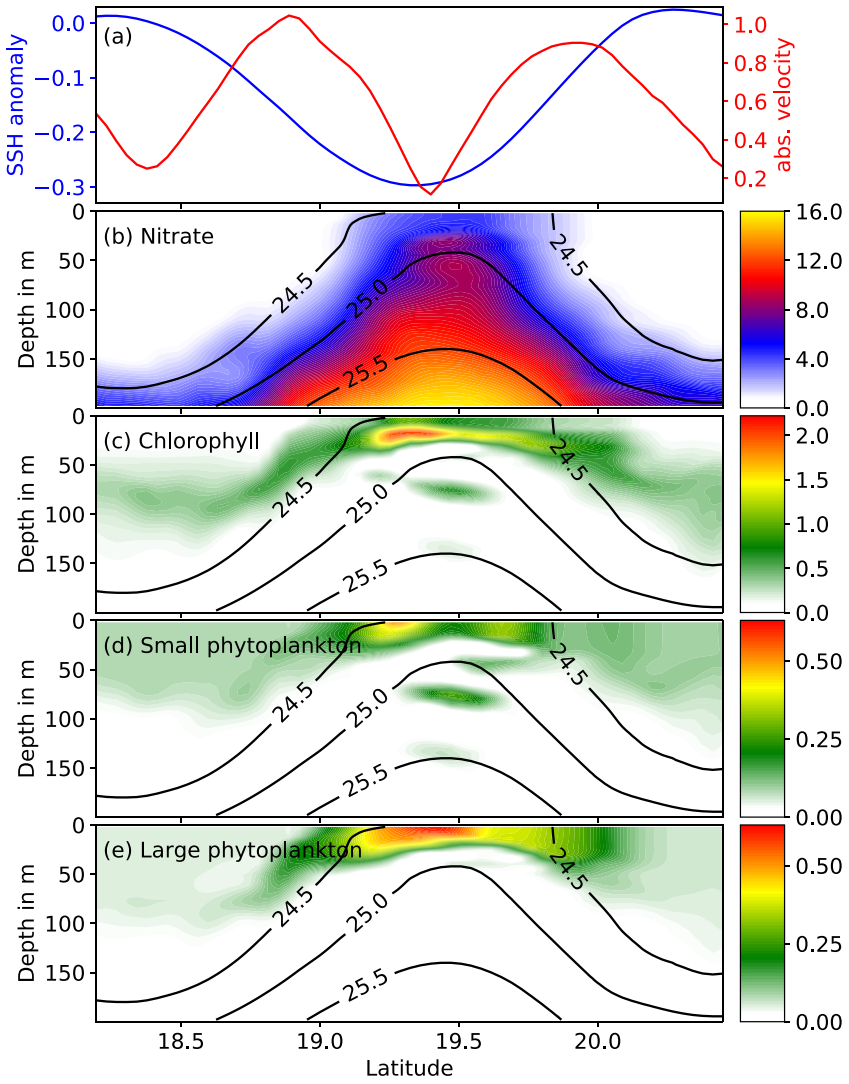

Figure 10. Meridional section across simulated cyclonic eddy to the west of the island of Hawaii as shown in Figure 1. Top panel: Simulated SSH anomaly in m (blue line, left hand axis) and absolute value of velocity in m s^{-1} (red line, right hand axis). Panel (b) Simulated nitrate concentrations (μmol kg^{-1}); (c) simulated chlorophyll (μg kg^{-1}); (d) simulated small phytoplankton concentration (μmol N kg^{-1}), and (e) simulated large phytoplankton concentration (μmol N kg^{-1}). Black lines in panels (b)–(e) indicate depths of simulated isopycnals (kg m^{-3}).

ecosystem to the west of Hawaii for the entire year 2013 is depicted in Figure 11, including the strong cyclonic eddy discussed above. It can be seen that the year is characterized by the passage of two cyclonic and two anticyclonic eddies. Even though the SSH anomalies for both cyclonic eddies are similar (Figure 11a), the doming of isopycnals and hence the nutrient supply to the euphotic zone is substantially smaller for the cyclonic eddy occurring later in the year (Figure 11c). The phytoplankton dynamics in both eddies turn out to be very different. The first 2 weeks of the cyclonic eddy occurring in March are characterized by a surface increase in both small and large phytoplankton (Figures 11d and 11e). After this initial phase, small phytoplankton is removed by grazing (not shown) and abruptly replaced by large phytoplankton. This shift demonstrates that the timing of transects might be crucial when gathering ship-based data of ecosystem dynamics in eddies. The contribution by large phytoplankton to the total phytoplankton biomass reaches more than 70% (Figure 11b) whereas the contribution by small phytoplankton drops to below 30% during this shift. The diazotroph contribution decreases from ~12% to below 3% during the passage of the cyclonic eddy.

Table 2
Simulated and observed Rates of N_2 Fixation (mmol N m^{-2} yr^{-1}) at Station ALOHA

This study	Fennel et al. (2002)	Karl et al. (1997)	Church et al. (2009)
38.6–71.5	26.7–54.3	31 ± 18–51 ± 26	41.3 ± 24.1

During the second cyclonic eddy, a different dynamics are observed. Despite the similarities in SSH evolution, the increase in nitrate supply is not as pronounced and consequently phytoplankton concentrations only rise slightly and at deeper layers of 30–70 m. Circulation-induced NPP is also substantially different for both eddies. The first eddy contributes a total of ~28% to the annual NPP (in the location shown) whereas the second cyclonic eddy contributes only 17%.

The passage of the two anticyclonic eddies results in a downward displacement of the isopycnals and a decrease in nitrate concentrations (Figure 11c). This is associated with a slight reduction in both small and large pythoplankton biomass. Maxima in diazotroph biomass coincide with the passage of the two anticyclonic eddies with the one occurring in the month of October being significantly more pronounced (Figure 11b). The complexity of the simulated temporal evolution in this highly dynamic region to the west of the island of Hawaii is a good example how continuous model output can complement the understanding of processes derived from observational transects.

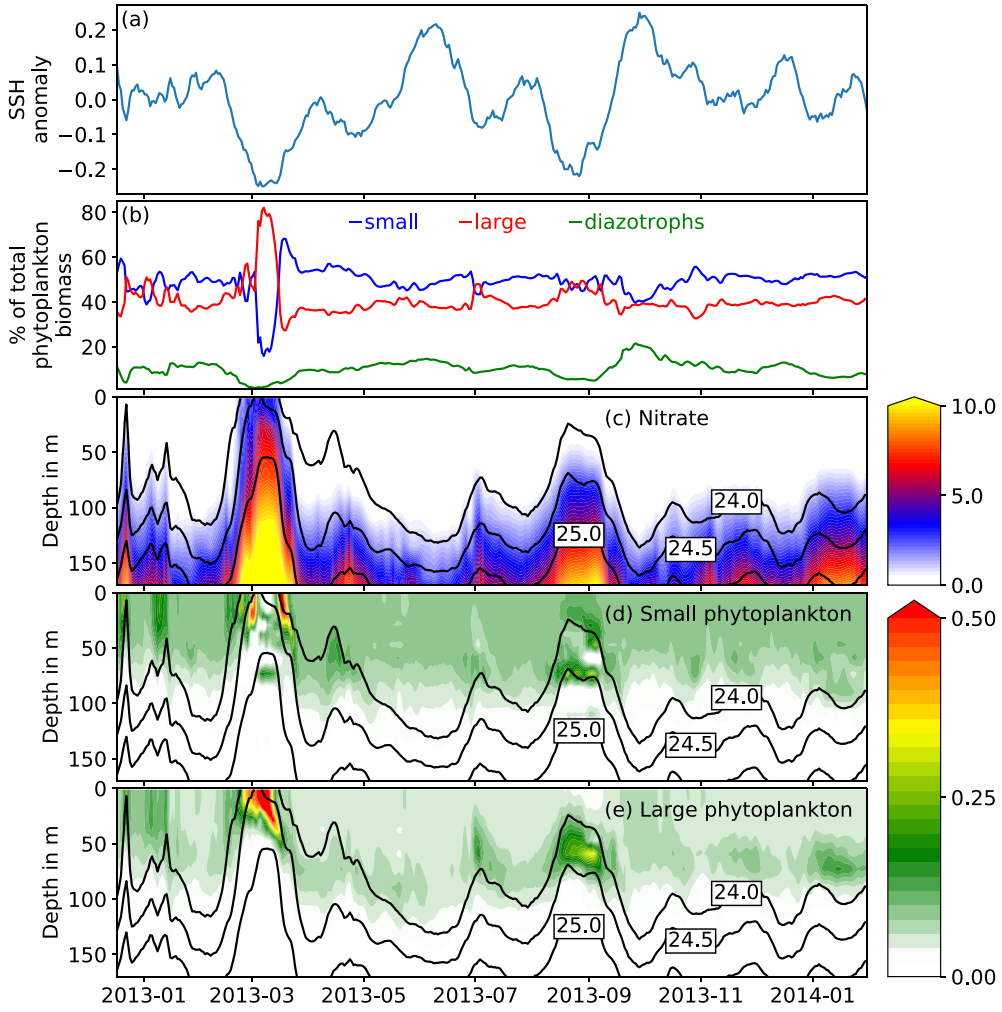

Figure 11. Simulated eddy-induced nitrate and phytoplankton variability to the west of the island of Hawaii for the year 2013. (a) Simulated sea surface height anomaly (m). (b) Contribution by simulated phytoplankton classes to total phytoplankton biomass (%): small (blue), large (red), and diazotrophs (green). (c) Nitrate concentration (μmol kg^{-1}). (d) Simulated small phytoplankton (μmol N kg^{-1}). (e) simulated large phytoplankton (μmol N kg^{-1}). Black lines in panels (c)–(e) indicate the depths of the 24.0, 24.5, and 25.0 km m^{-3} isopycnals, respectively. Spatial averaging was applied for 11 grid points in longitude and latitude centered around 19.44°N/156.73°W. Please see pink rectangle in Figure 1.

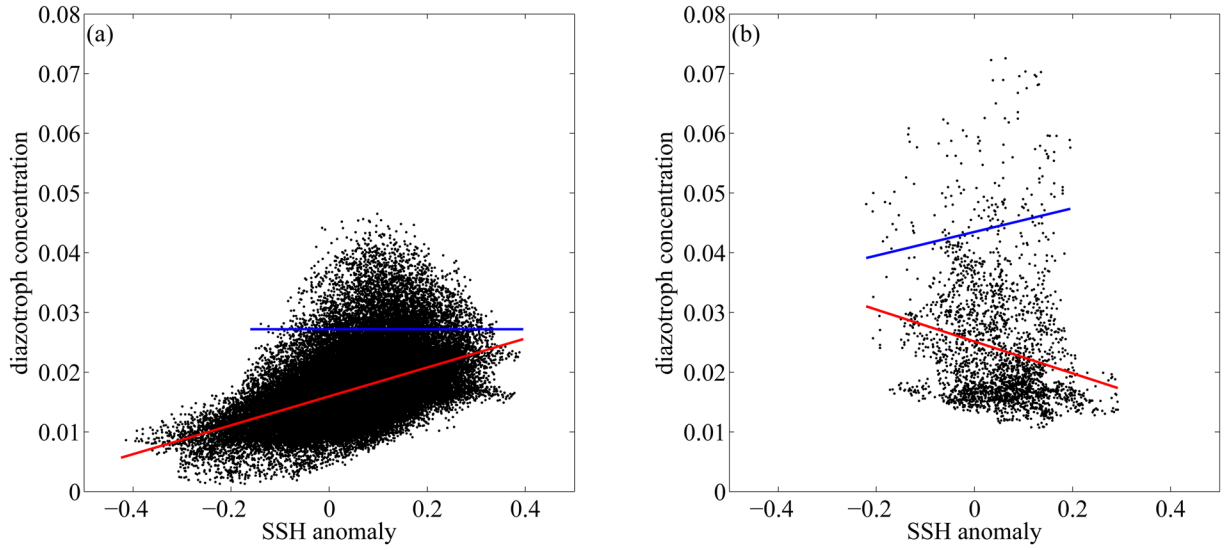

Figure 12. Relationship between SSH anomalies and diazotroph concentrations. (a) Simulated diazotroph concentrations (μmol N kg^{-1}) versus SSH anomalies (m) for the region west of the island of Hawaii. Red line indicates a linear fit for all data shown. Blue line indicates a linear fit for diazotroph concentrations greater than one standard deviation above the time average. (b) Same as in (a) for Station ALOHA.

Results of observational studies at Station ALOHA are indicative of increased nitrogen fixation occurring during periods of positive SSH anomalies (Böttjer et al., 2017; Church et al., 2009; Fong et al., 2008). Using our model output, we have tested a potential SSH-nitrogen fixation relationship for the region west of the island of Hawaii (where SSH anomalies are typically the largest) and for Station ALOHA. Based on the entire simulation, the correlation between SSH anomalies and vertically averaged (0–100 m) diazotroph concentrations amounts to 0.45 for the region west of the island of Hawaii (Figure 12a). This correlation, however, varies greatly between different model years with a range of 0.12–0.69 and does not warrant robust conclusions. For the Station ALOHA location, it can be seen that SSH anomalies are smaller while vertically averaged diazotroph concentrations reach larger values (Figure 12b). Using all model years, the correlation between SSH anomalies and vertically averaged diazotroph concentrations amounts to −0.22 but varies from year to year with a range of −0.52–0.32. Based on 9 years of measurements, Böttjer et al. (2017) concluded that N_2-fixation rates above one standard deviation above the mean coincided largely with the passage of anticyclonic eddies and the associated positive SSH anomalies. Limiting the simulated data to diazotroph concentrations greater than one standard deviation above the time average, the slope of the linear fit becomes positive. However, the correlation of $r = 0.18$ is very small and does not allow for a meaningful interpretation.

The location of the maxima/minima of the EOF2 and EOF3 of NPP is not only found to the west of the island of Hawaii but also to the north of Molokai and Maui (Figures 7b and 7c). The northeast side of the MHI is subject to sporadic, localized upwelling driven by the trade winds and the interaction of the North Equatorial Current with the island topography. This island mass effect (Doty & Oguri, 1956; Gove et al., 2016) can supply nutrients to the euphotic zone. Figure 13 shows a meridional section off the north shore of Molokai for late November 2011. The nearshore SST is about 1 °C colder corresponding to an outcropping of the 23 °C isotherm that is found at a depth of ~80 m further offshore. Surface nitrate concentrations are strongly enhanced near the island reaching values of 2 μmol kg^{-1} compared to values well below 0.1 μmol kg^{-1} further to the north. Part of the upwelled nitrate is horizontally advected in a local near-surface loop current (not shown), creating a second peak in nitrate concentrations at about 60–80 km offshore. The spatial structure of near-surface chlorophyll and NPP follows the pattern of nitrate concentrations with substantially increased NPP (and chlorophyll concentration) within 10 km of the island and a second offshore peak (Figure 13a). Upwelling increases near-shore chlorophyll concentrations by more than 300% compared to offshore values for this upwelling event. The corresponding increase in NPP is of similar magnitude.

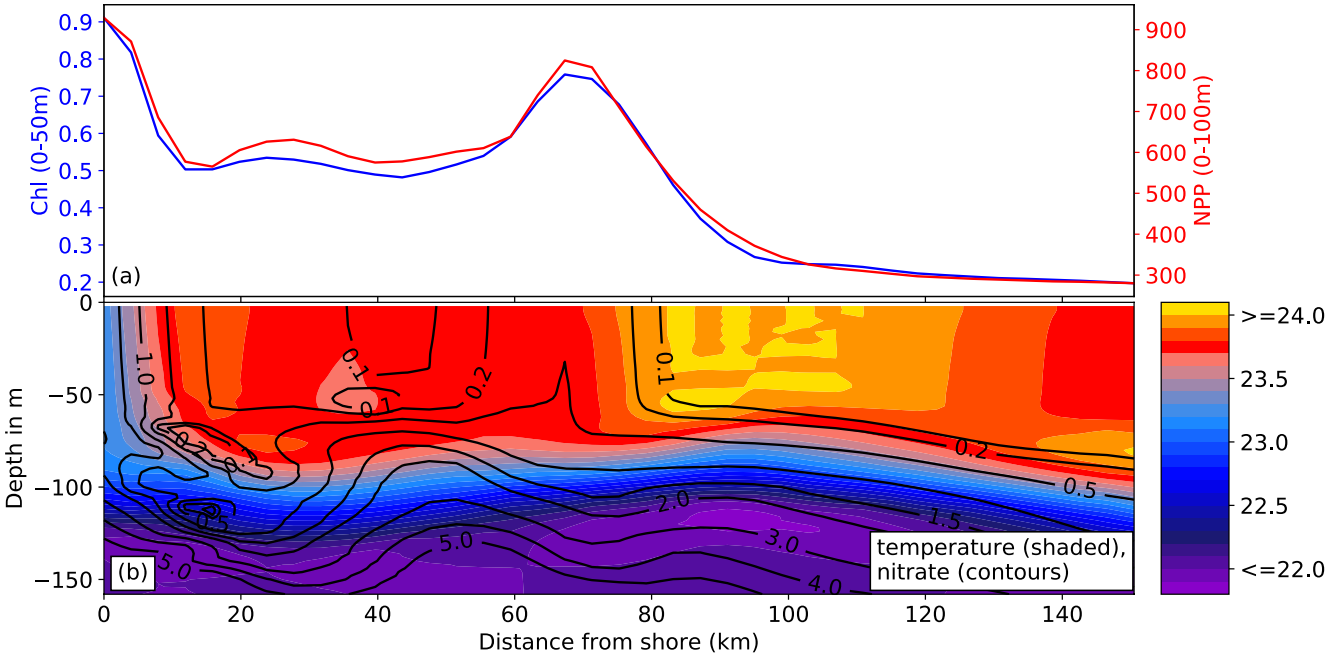

Figure 13. Island mass effect: Meridional section off the north shore of Molokai (156.88°W). See orange line in Figure 1 for location. (a) Near-surface chlorophyll (μg kg^{-1}, blue line) and NPP integrated 0–100 m (mg C m^{-2} d^{-1}, red line). (b) temperature (°C, shaded) and nitrate concentration (μmol kg^{-1}, contours).

Taking into account the entire period of our simulation and all of the MHI, it can be seen that the topographic outcropping leads to an average increase of 4%–10% in nearshore chlorophyll concentrations (Figure 14a). The main contribution comes from the islands of Maui and Molokai with increase rates of 15%–

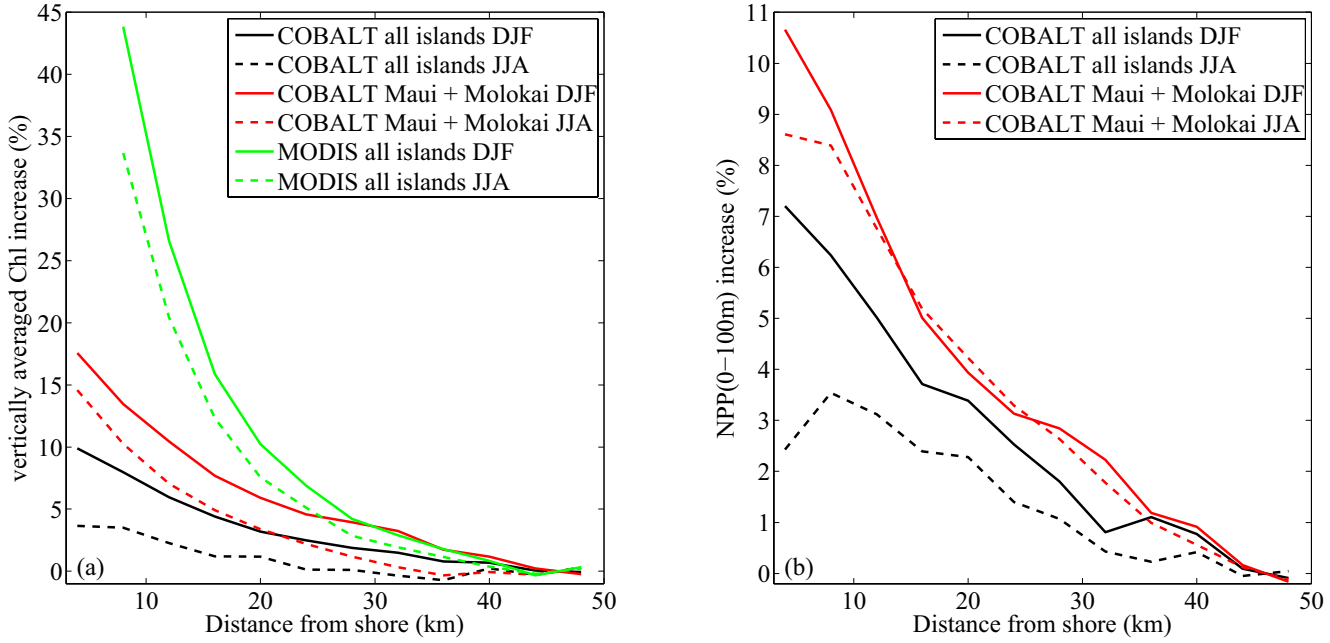

Figure 14. Island mass effect for chlorophyll and net primary production for summer (JJA) and winter (DJF) months. (a) Vertically averaged chlorophyll increase (%) versus distance from shore (km) for all islands (black) and Maui county (red) and MODIS (all islands, green). (b) Depth-integrated (0–100 m) net primary production increase (%) versus distance from shore (km) for all islands (black) and Maui county (red). Solid lines indicate DJF, and dashed lines indicate JJA data.

20% whereas the remaining islands see increases of less than 5% (not shown). The island-wide nearshore increase in NPP ranges between 2% in summer and 7% in winter (Figure 14b).

When calculating the island mass effect for MODIS chlorophyll data, it must be kept in mind that accuracy of ocean color data in the nearshore environment is not guaranteed and that results should be interpreted with caution. When excluding points closer than 8 km to shore from our analysis, it becomes evident that our simulation underestimates the overall nearshore chlorophyll increase by a factor of three (Figure 14a). One reason for this discrepancy can be found in the fact that terrestrial nutrient input is not taken into account in the current set-up. Furthermore, certain coastal features cannot be represented in a 4 km resolution. Lastly, the model's capacity to simulate elevated nearshore chlorophyll concentrations might be hampered by a limited representation of the phytoplankton community structure. The spatial extent of the island mass effect simulated by our model is on average approximately 30 km and is in good agreement with the MODIS data and values presented by Gove et al. (2016). It should be noted, however, that nearshore advection of nutrients and chlorophyll as well as the occurrence of phytoplankton-laden eddies in the vicinity of the islands can complicate the computation of the spatial extent of the island mass effect.

The physical mechanisms behind the island mass effect such as sporadic wind- and current-driven nearshore upwelling of colder waters occur throughout the year and do not show indication of seasonality. This island mass effect, however, is more pronounced during winter season (DJF) compared to summer (JJA) for both our simulation as well as the MODIS chlorophyll data (Figure 14a). Our analysis reveals that the summertime nitracline is approximately 20 m deeper resulting in lower nutrient concentrations of the upwelled water. This result is in good agreement with measurements presented by L. M. Letelier et al. (2004), and we speculate that it is also the main reason behind the stronger winter increase seen in the MODIS chlorophyll data. However, an additional effect of terrestrial runoff cannot be ruled out. The latter is typically stronger during winter (wet) season and would result in an enhanced coastal nutrient input not taken into account in our model simulation.

4. Conclusions and Perspective

Our simulations have identified three major provinces and four critical processes for phytoplankton blooms around the main Hawaiian islands. The oligotrophic open ocean regions are characterized by a seasonal deepening of light levels across the spring nutricline as well as nitrogen fixation during late summer stratification of the water column. The southwestern side of the MHI—in particular the west of the island of Hawaii—is home to cyclonic eddies in which isopycnal doming can increase nutrient concentrations in the euphotic zone by up to 100 times. The immediate vicinity of the islands exhibits an island mass effect due to wind- and current-driven upwelling of nutrient-rich water especially on the north shores of Molokai and Maui.

Embedding the model in a physical state estimate and using high-resolution atmospheric forcing has allowed for a realistic incorporation of ocean physics and has resulted in a good agreement between simulated and observed physical and biogeochemical parameters. Our results show that the model can be used as a one-of-a-kind tool to complement measurements and to test hypotheses arising from observational data. In particular, the understanding of processes occurring on shorter timescales not covered by the HOT program can be improved through the use of model data. Furthermore, continuous three-dimensional model output can help put into context measurements gathered during individual transects and other snapshot observations.

In addition to complementing observational data, the presented model can be used to carry out more robust future projections for the main Hawaiian islands. Given that current global climate models cannot capture the dynamic circulation features around the islands, our high-resolution regional model will be a unique tool to capture both the natural variability as well as the anthropogenic trend in physical and biogeochemical variables.

The model resolution, setup, and parameterizations will be further improved in the future. The simulation of the DCML at Station ALOHA—which is currently too shallow—will be addressed by refining the dynamical chlorophyll-to-carbon ratio and by increasing the vertical resolution of the model. The latter will also

help to enhance the representation of vertical profiles in water depths of 400–1,000 m where the current spacing of model grid points leads to a smoothing of vertical gradients.

Another shortcoming of the present setup is the use of climatological biogeochemical boundary conditions as well as the lack of varying atmospheric iron input which hampers the representation of interannual variability of phytoplankton blooms. Taking into account terrestrial nutrient inputs will likely result in a better capturing of the island mass effect. The role of frontogenesis and straining in promoting phytoplankton blooms has been neglected here and will be the focus of a future study using a higher model resolution.

Conflict of Interest

The authors declare no conflicts of interest relevant to this study.

Data Availability Statement

Simulated and observational data shown in the figures can be found at https://osf.io/ej8kn/(last access: 23 March 2021). Raw observational data presented in this study are available through: http://hahana.soest.hawaii.edu/hot/(last access: 23 March 2021) and through: https://oceandata.sci.gsfc.nasa.gov/MODIS-Aqua/Mapped/8-Day/4km/chlor_a/(last access: 23 March 2021). Please contact the corresponding author to obtain access to the raw model outputs.

Acknowledgments
This work was supported by the Pacific Islands Ocean Observing System (PacIOOS, http://www.pacioos.hawaii.edu, last access: 23 March 2021), which is a part of the US Integrated Ocean Observing System (IOOS®), funded in part by National Oceanic and Atmospheric Administration (NOAA) Award No. NA16NOS0120024. Lisa Hahn-Woernle was supported by the Joint Institute for Marine and Atmospheric Research (JIMAR, http://www.soest.hawaii.edu/jimar/, last access: 23 March 2021). The authors would like to thank the Hawaii Ocean Time-series (HOT) project for their continuous efforts to carry out ocean observations around the Hawaiian Islands. The authors would like to thank the Editor Marjorie Friedrichs and the three anonymous reviewers for their comments that helped improve the manuscript. This is SOEST publication number 11341.

References

Ascani, F., Richards, K. J., Firing, E., Grant, S., Johnson, K. S., Jia, Y., et al. (2013). Physical and biological controls of nitrate concentrations in the upper subtropical North Pacific Ocean. *Deep Sea Research Part II: Topical Studies in Oceanography*, *93*, 119–134. https://doi.org/10.1016/j.dsr2.2013.01.034

Baron de Fourier, J. B. J. (1822). *Théorie analytique de la chaleur*. Firmin Didot.

Böttjer, D., Dore, J. E., Karl, D. M., Letelier, R. M., Mahaffey, C., Wilson, S. T., et al. (2017). Temporal variability of nitrogen fixation and particulate nitrogen export at Station ALOHA. *Limnology & Oceanography*, *62*(1), 200–216. https://doi.org/10.1002/lno.10386

Brown, S. L., Landry, M. R., Selph, K. E., Yang, E. J., Rii, Y. M., & Bidigare, R. (2008). Diatoms in the desert: Plankton community response to a mesoscale eddy in the subtropical North Pacific. *Deep Sea Research Part II: Topical Studies in Oceanography*, *55*(10–13), 1321–1333. https://doi.org/10.1016/j.dsr2.2008.02.012

Calil, P. H. R., & Richards, K. J. (2010). Transient upwelling hot spots in the oligotrophic North Pacific. *Journal of Geophysical Research: Oceans*, *115*(C2). https://doi.org/10.1029/2009jc005360

Calil, P. H. R., Richards, K. J., Jia, Y., & Bidigare, R. R. (2008). Eddy activity in the lee of the Hawaiian Islands. *Deep Sea Research Part II: Topical Studies in Oceanography*, *55*(10–13), 1179–1194. https://doi.org/10.1016/j.dsr2.2008.01.008

Campbell, L., & Vaulot, D. (1993). Photosynthetic picoplankton community structure in the subtropical North Pacific Ocean near Hawaii (station ALOHA). *Deep Sea Research Part I: Oceanographic Research Papers*, *40*(10), 2043–2060. https://doi.org/10.1016/0967-0637(93)90044-4

Capone, D. G., Zehr, J. P., Paerl, H. W., Bergman, B., & Carpenter, E. J. (1997). Trichodesmium, a globally significant marine cyanobacterium. *Science*, *276*(5316), 1221–1229. https://doi.org/10.1126/science.276.5316.1221

Chavanne, C., Flament, P., Lumpkin, R., Dousset, B., & Bentamy, A. (2002). Scatterometer observations of wind variations induced by oceanic islands: Implications for wind-driven ocean circulation. *Canadian Journal of Remote Sensing*, *28*(3), 466–474. https://doi.org/10.5589/m02-047

Church, M. J., Mahaffey, C., Letelier, R. M., Lukas, R., Zehr, J. P., & Karl, D. M. (2009). Physical forcing of nitrogen fixation and diazotroph community structure in the North Pacific subtropical gyre. *Global Biogeochemical Cycles*, *23*(2). https://doi.org/10.1029/2008gb003418

Cooley, J. W., & Tukey, J. W. (1965). An algorithm for the machine calculation of complex fourier series. *Mathematics of Computation*, *19*(90), 297. https://doi.org/10.1090/s0025-5718-1965-0178586-1

de Boyer Montégut, C., Madec, G., Fischer, A. S., Lazar, A., & Iudicone, D. (2004). Mixed layer depth over the global ocean: An examination of profile data and a profile-based climatology. *Journal of Geophysical Research: Oceans*, *109*(C12). https://doi.org/10.1029/2004jc002378

Dore, J. E., Brum, J. R., Tupas, L. M., & Karl, D. M. (2002). Seasonal and interannual variability in sources of nitrogen supporting export in the oligotrophic subtropical North Pacific Ocean. *Limnology & Oceanography*, *47*(6), 1595–1607. https://doi.org/10.4319/lo.2002.47.6.1595

Doty, M. S., & Oguri, M. (1956). The island mass effect. *ICES Journal of Marine Science*, *22*(1), 33–37. https://doi.org/10.1093/icesjms/22.1.33

Dussin, R., Curchitser, E., Stock, C., & Van Oostende, N. (2019). Biogeochemical drivers of changing hypoxia in the California Current Ecosystem. *Deep Sea Research Part II: Topical Studies in Oceanography*, *169*, 104590.

Egbert, G. D., Bennett, A. F., & Foreman, M. G. G. (1994). TOPEX/POSEIDON tides estimated using a global inverse model. *Journal of Geophysical Research*, *99*(C12), 24821–24852. https://doi.org/10.1029/94JC01894

Fennel, K., Spitz, Y. H., Letelier, R. M., Abbott, M. R., & Karl, D. M. (2002). A deterministic model for N2 fixation at stn. ALOHA in the subtropical North Pacific Ocean. *Deep Sea Research Part II: Topical Studies in Oceanography*, *49*(1–3), 149–174.

Fong, A. A., Karl, D. M., Lukas, R., Letelier, R. M., Zehr, J. P., & Church, M. J. (2008). Nitrogen fixation in an anticyclonic eddy in the oligotrophic North Pacific Ocean. *The ISME Journal*, *2*(6), 663–676. https://doi.org/10.1038/ismej.2008.22

Geider, R., MacIntyre, H., & Kana, T. (1997). Dynamic model of phytoplankton growth and acclimation: Responses of the balanced growth rate and the chlorophyll a: Carbon ratio to light, nutrient-limitation and temperature. *Marine Ecology Progress Series*, *148*, 187–200. https://doi.org/10.3354/meps148187

Goebel, N. L., Edwards, C. A., Church, M. J., & Zehr, J. P. (2007). Modeled contributions of three types of diazotrophs to nitrogen fixation at Station ALOHA. *The ISME Journal*, *1*(7), 606–619. https://doi.org/10.1038/ismej.2007.80

Gove, J. M., McManus, M. A., Neuheimer, A. B., Polovina, J. J., Drazen, J. C., Smith, C. R., et al. (2016). Near-island biological hotspots in barren ocean basins. *Nature Communications*, *7*(1), 1–8. https://doi.org/10.1038/ncomms10581

Hitzl, D. E., Chen, Y.-L., & Van Nguyen, H. (2014). Numerical Simulations and Observations of Airflow through the 'Alenuihāhā Channel, Hawaii. *Hawaii. Monthly Weather Review*, *142*(12), 4696–4718. https://doi.org/10.1175/mwr-d-13-00312.1

HMRG. (2017). *Hawaii Mapping Research Group*. University of Hawaii. Retrieved from http://www.soest.hawaii.edu/HMRG/multibeam/index.php

Jia, Y., Calil, P. H. R., Chassignet, E., Metzger, E., Potemra, J., Richards, K., & Wallcraft, A. J. (2011). Generation of mesoscale eddies in the lee of the Hawaiian Islands. *Journal of Geophysical Research: Oceans*, *116*(C11). https://doi.org/10.1029/2011jc007305

Johnson, K. S., Riser, S. C., & Karl, D. M. (2010). Nitrate supply from deep to near-surface waters of the North Pacific subtropical gyre. *Nature*, *465*(7301), 1062–1065. https://doi.org/10.1038/nature09170

Karl, D., Letelier, R., Tupas, L., Dore, J., Christian, J., & Hebel, D. (1997). The role of nitrogen fixation in biogeochemical cycling in the subtropical North Pacific Ocean. *Nature*, *388*(6642), 533–538. https://doi.org/10.1038/41474

Karl, D. M., & Church, M. J. (2017). Ecosystem structure and dynamics in the North Pacific Subtropical Gyre: New views of an old ocean. *Ecosystems*, *20*(3), 433–457. https://doi.org/10.1007/s10021-017-0117-0

Karl, D. M., & Church, M. J. (2018). Station ALOHA: A gathering place for discovery, education, and scientific collaboration. *Limnology and Oceanography Bulletin*, *28*, 10–12. https://doi.org/10.1002/lob.10285

Karl, D. M., & Lukas, R. (1996). The Hawaii Ocean Time-series (HOT) program: Background, rationale and field implementation. *Deep Sea Research Part II: Topical Studies in Oceanography*, *43*(2–3), 129–156. https://doi.org/10.1016/0967-0645(96)00005-7

Keeling, C. D., Bacastow, R. B., Bainbridge, A. E., Ekdahl Jr, C. A., Jr, Guenther, P. R., Waterman, L. S., & Chin, J. F. S. (1976). Atmospheric carbon dioxide variations at Mauna Loa observatory, Hawaii. *Tellus*, *28*(6), 538–551. https://doi.org/10.3402/tellusa.v28i6.11322

Keeling, C. D., Brix, H., & Gruber, N. (2004). Seasonal and long-term dynamics of the upper ocean carbon cycle at station aloha near hawaii. *Global Biogeochemical Cycles*, *18*(4). https://doi.org/10.1029/2004gb002227

Kuwahara, V. S., Nencioli, F., Dickey, T. D., Rii, Y. M., & Bidigare, R. R. (2008). Physical dynamics and biological implications of Cyclone Noah in the lee of Hawaii during E-Flux I. *Deep Sea Research Part II: Topical Studies in Oceanography*, *55*(10–13), 1231–1251. https://doi.org/10.1016/j.dsr2.2008.01.007

Letelier, R., & Karl, D. (1996). Role of Trichodesmium spp. in the productivity of the subtropical North Pacific Ocean. *Marine Ecology Progress Series*, *133*, 263–273. https://doi.org/10.3354/meps133263

Letelier, R. M., Bidigare, R. R., Hebel, D. V., Ondrusek, M., Winn, C. D., & Karl, D. M. (1993). Temporal variability of phytoplankton community structure based on pigment analysis. *Limnology & Oceanography*, *38*(7), 1420–1437. https://doi.org/10.4319/lo.1993.38.7.1420

Letelier, R. M., Björkman, K. M., Church, M. J., Hamilton, D. S., Mahowald, N. M., Scanza, R. A., et al. (2019). Climate-driven oscillation of phosphorus and iron limitation in the North Pacific Subtropical Gyre. *Proceedings of the National Academy of Sciences of the United States of America*, *116*(26), 12720–12728. https://doi.org/10.1073/pnas.1900789116

Letelier, R. M., Karl, D. M., Abbott, M. R., & Bidigare, R. R. (2004). Light driven seasonal patterns of chlorophyll and nitrate in the lower euphotic zone of the North Pacific Subtropical Gyre. *Limnology & Oceanography*, *49*(2), 508–519. https://doi.org/10.4319/lo.2004.49.2.0508

Manizza, M., Le Quéré, C., Watson, A. J., & Buitenhuis, E. T. (2008). Ocean biogeochemical response to phytoplankton-light feedback in a global model. *Journal of Geophysical Research: Oceans*, *113*(C10). https://doi.org/10.1029/2007jc004478

Moore, A. M., Arango, H. G., Broquet, G., Edwards, C., Veneziani, M., Powell, B., et al. (2011). The Regional Ocean Modeling System (ROMS) 4-dimensional variational data assimilation systems. *Progress in Oceanography*, *91*(1), 74–94. https://doi.org/10.1016/j.pocean.2011.05.005

Moore, A. M., Arango, H. G., Broquet, G., Edwards, C., Veneziani, M., Powell, B., et al. (2011a). The Regional Ocean Modeling System (ROMS) 4-dimensional variational data assimilation systems. *Progress in Oceanography*, *91*(1), 50–73. https://doi.org/10.1016/j.pocean.2011.05.003

Moore, A. M., Arango, H. G., Broquet, G., Powell, B. S., Weaver, A. T., & Zavala-Garay, J. (2011b). The Regional Ocean Modeling System (ROMS) 4-dimensional variational data assimilation systems. *Progress in Oceanography*, *91*(1), 34–49. https://doi.org/10.1016/j.pocean.2011.05.004

NASA Goddard Space Flight Center, Ocean Ecology Laboratory, Ocean Biology Processing Group. (2018). *Moderate-Resolution Imaging Spectroradiometer (MODIS) Aqua Chlorophyll Data; 2018 Reprocessing* (Tech. Rep.). data/https://doi.org/10.5067/AQUA/MODIS/L3B/CHL/2018

Nencioli, F., Kuwahara, V. S., Dickey, T. D., Rii, Y. M., & Bidigare, R. R. (2008). Physical dynamics and biological implications of a mesoscale eddy in the lee of Hawaii: Cyclone Opal observations during E-Flux III. *Deep Sea Research Part II: Topical Studies in Oceanography*, *55*(10–13), 1252–1274. https://doi.org/10.1016/j.dsr2.2008.02.003

Partensky, F., & Garczarek, L. (2010). Prochlorococcus: Advantages and limits of minimalism. *Annual Review of Marine Science*, *2*, 305–331. https://doi.org/10.1146/annurev-marine-120308-081034

Partridge, D., Friedrich, T., & Powell, B. S. (2019). Reanalysis of the PacIOOS Hawaiian Island Ocean Forecast System, an implementation of the Regional Ocean Modeling System v3.6. *Geoscientific Model Development*, *12*(1), 195–213. https://doi.org/10.5194/gmd-12-195-2019

Patzert, W. C. (1969). *Eddies in Hawaiian waters (Tech. Rep. No. HIG-69-8)*. Hawaii Institute of Geophysics, University of Hawaii.

Powell, B. S., Arango, H. G., Moore, A. M., Di Lorenzo, E., Milliff, R. F., & Foley, D. (2008). 4DVAR data assimilation in the Intra-Americas Sea with the regional ocean modeling system (ROMS). *Ocean Modelling*, *25*, 173–188. https://doi.org/10.1016/j.ocemod.2008.08.002

Redfield, A. C. (1963). The influence of organisms on the composition of seawater. *The Sea*, *2*, 26–77.

Rii, Y. M., Brown, S. L., Nencioli, F., Kuwahara, V., Dickey, T., Karl, D. M., & Bidigare, R. R. (2008). The transient oasis: Nutrient-phytoplankton dynamics and particle export in Hawaiian lee cyclones. *Deep Sea Research Part II: Topical Studies in Oceanography*, *55*(10–13), 1275–1290. https://doi.org/10.1016/j.dsr2.2008.01.013

Roman, M., Adolf, H., Landry, M., Madin, L., Steinberg, D., & Zhang, X. (2001). Estimates of oceanic mesozooplankton production: A comparison using the bermuda and hawaii time-series data. *Deep Sea Research Part II: Topical Studies in Oceanography*, *49*(1–3), 175–192. https://doi.org/10.1016/s0967-0645(01)00099-6

Shchepetkin, A. F., & McWilliams, J. C. (1998). Quasi-monotone advection schemes based on explicit locally adaptive dissipation. *Monthly Weather Review*, *126*(6), 1541–1580. https://doi.org/10.1175/1520-0493(1998)126<1541:qmasbo>2.0.co;2

Shchepetkin, A. F., & McWilliams, J. C. (2003). A method for computing horizontal pressure-gradient force in an oceanic model with a nonaligned vertical coordinate. *Journal of Geophysical Research*, *108*(C3). 3090. https://doi.org/10.1029/2001JC001047

Shchepetkin, A. F., & McWilliams, J. C. (2005). The regional oceanic modeling system (ROMS): A split-explicit, free-surface, topography-following-coordinate oceanic model. *Ocean Modelling*, *9*(4), 347–404. https://doi.org/10.1016/j.ocemod.2004.08.002

Smith, S. L., Yamanaka, Y., & Kishi, M. J. (2005). Attempting consistent simulations of Stn. ALOHA with a multi-element ecosystem model. *Journal of Oceanography*, *61*(1), 1–23.

Souza, J. M. A. C., Powell, B. S., Castillo-Trujillo, A. C., & Flament, P. (2015). The Vorticity Balance of the Ocean Surface in Hawaii from a Regional Reanalysis. *Journal of Physical Oceanography*, *45*(2), 424–440. https://doi.org/10.1175/JPO-D-14-0074.1

Stock, C., & Dunne, J. (2010). Controls on the ratio of mesozooplankton production to primary production in marine ecosystems. *Deep Sea Research Part I: Oceanographic Research Papers*, *57*(1), 95–112. https://doi.org/10.1016/j.dsr.2009.10.006

Stock, C. A., Dunne, J. P., & John, J. G. (2014). Global-scale carbon and energy flows through the marine planktonic food web: An analysis with a coupled physical-biological model. *Progress in Oceanography*, *120*, 1–28. https://doi.org/10.1016/j.pocean.2013.07.001

Sunda, W. G., & Huntsman, S. A. (1997). Interrelated influence of iron, light and cell size on marine phytoplankton growth. *Nature*, *390*(6658), 389–392. https://doi.org/10.1038/37093

Thompson, A. W., Kouba, K., & Ahlgren, N. A. (2021). Niche partitioning of low-light adapted prochlorococcus subecotypes across oceanographic gradients of the north pacific subtropical front. *Limnology and Oceanography*, *66*(4), 1548–1562.

Vaillancourt, R. D., Marra, J., Seki, M. P., Parsons, M. L., & Bidigare, R. R. (2003). Impact of a cyclonic eddy on phytoplankton community structure and photosynthetic competency in the subtropical North Pacific Ocean. *Deep Sea Research Part I: Oceanographic Research Papers*, *50*(7), 829–847. https://doi.org/10.1016/s0967-0637(03)00059-1

Van Oostende, N., Dussin, R., Stock, C. A., Barton, A. D., Curchitser, E., Dunne, J. P., & Ward, B. B. (2018). Simulating the ocean's chlorophyll dynamic range from coastal upwelling to oligotrophy. *Progress in Oceanography*, *168*, 232–247. https://doi.org/10.1016/j.pocean.2018.10.009

Wilson, S. T., Hawco, N. J., Armbrust, E. V., Barone, B., Björkman, K. M., Boysen, A. K., et al. (2019). Kīlauea lava fuels phytoplankton bloom in the North Pacific Ocean. *Science*, *365*(6457), 1040–1044. https://doi.org/10.1126/science.aax4767

Xie, S.-P., Liu, W. T., Liu, Q., & Nonaka, M. (2001). Far-reaching effects of the Hawaiian Islands on the Pacific ocean-atmosphere system. *Science*, *292*(5524), 2057–2060. https://doi.org/10.1126/science.1059781

Zhang, S., Curchitser, E. N., Kang, D., Stock, C. A., & Dussin, R. (2018). Impacts of mesoscale eddies on the vertical nitrate flux in the Gulf stream region. *Journal of Geophysical Research: Oceans*, *123*(1), 497–513. https://doi.org/10.1002/2017jc013402